2022

Synthesis and modeling of manganese ferrite nanoparticles for magnetic hyperthermia applications

Margaret E. Thornton

Synthesis and modeling of manganese ferrite nanoparticles for magnetic hyperthermia applications

A dissertation submitted in partial fulfillment of the requirements for the degree of Doctor of Philosophy at Virginia Commonwealth University.

By

Margaret E. Thornton
B.S., Virginia Commonwealth University, 2018

Advisor: Dr. Everett E. Carpenter, Professor of Chemistry

Virginia Commonwealth University

Richmond, VA

May 2022

Acknowledgements

There are a number of individuals that were influential to my academic journey, whose wisdom, humor, and advice have shaped me into the scientist and person I am today. I carry endless gratitude for all: Professor Hamelman, for making math make sense, Dr. Jenson, for the votes of confidence and good conversation, Dr. Turner, for sharing in my interests in all things equine and instruments, and Dr. Luzar and Dr. Bratko, for encouraging and supporting the enthusiastic undergraduate. Thank you to my committee members, Dr. Bertino, Dr. Bratko, and Dr. Tibbetts, for always asking the hard questions, and most importantly, thank you to Dr. Carpenter for the endless patience, support, and assurance. I could not be more thankful to have such incredible mentors.

Contents

List of Figures

List of Tables

Abbreviations and Symbols

AC	Alternating current
CCP	Cubic closest packing
CFSE	Crystal field stabilization energy
EXAFS	X-Ray absorption fine structure
FEG	Field emission gun
FT-IR	Fourier transform infrared spectroscopy
FWHM	Full width half maximum
GP	Griffiths phase
IV	Intravenous
LA-ICP-MS	Laser ablation inductively coupled mass spectrometry
MFO	Manganese iron oxide
MH	Magnetic hyperthermia
MNPs	Magnetic nanoparticles
MRI	Magnetic resonance imaging
M_S	Saturation magnetization
PCA	Principal component analysis
PID	Proportional integral derivative
PPMS	Physical property measurement system
SAR	Specific absorption rate
SLP	Specific loss power
TEG	Tetraethylene glycol
TEM	Transmission electron microscopy
TGA	Thermal gravimetric analysis
UCL	Upper control limit
VSM	Vibrating sample magnetometry
XRD	X-ray diffraction

Abstract

Biologically targeted magnetic hyperthermia (MH) is a promising cancer therapeutic that is both non-invasive and has the potential to serve as a single-modality cancer treatment. MH operates through the elevation of temperatures between 40-43 °C to induce apoptosis in malignant tumor cells, while the small size of the magnetic nanoparticles preserves the healthy surrounding tissue. At present, MH is limited by low heating efficiency and heterogenous outcomes, and treatment requires direct-injection of the nanoparticles, excluding deep-tissue and metastatic tumors from the therapy.

The most popular candidates for MH are the spinel ferrites iron oxide and manganese iron oxide (MFO). These materials have been extensively discussed in the literature, but at present, no significant relationship has been identified between synthetic method, material properties, and *in vivo* efficacy. Synthesis at the nanoscale imparts a variety of novel properties on a material, and difficulty in characterizing many of these features has led to a poor understanding of how to tailor MFO for clinical applications. In order for MH to be realized as a standalone clinical theranostic, several variables must be targeted. In particular, the saturation magnetization (M_S) of the material must be maximized for *in vivo* applications.

M_S can be influenced by a variety of parameters that are highly dependent on synthetic condition. Synthetic modifications were made to a facile polyol route in order to build a material model of MFO using principal component analysis (PCA). Nanoparticles with average crystallite sizes ranging from 4.8 to 12.3 nm were synthesized through a variety of conditions and served as inputs for the PCA. This exploratory analysis aided in identifying which synthetic variations most influenced material properties. A subset of samples was selected based on the PCA results for further magnetic characterization, which enabled the identification of a single synthetic methodology that maximized M_S for the series.

This work addresses several inconsistencies in existing literature regarding MH candidates, and reports on the synthetic parameters necessary to maximize the M_S of MFO nanoparticles. It was found that synthetic conditions played the most significant role in altering material properties, while previously identified factors such as crystallite size were less influential. The optimized synthetic strategy presented herein serves as a blueprint for future work in enabling MH as a standalone treatment for cancer.

Chapter 1. Introduction to Magnetic Hyperthermia and Magnetic Nanoparticles

1.1 Overview

According to the World Health Organization, cancer is a leading cause of death worldwide, with the most common types being breast, lung, colon, and prostate.[1] While many types of cancer can be cured, oncology treatments are notorious for their unpleasant side effects, extended treatment times, and harsh treatment modalities. From the late 1800s, hyperthermia has been used as an oncogenic therapy as whole body, regional, or local.[2] As hyperthermia continues to gain traction as a cancer therapeutic, local treatments are being reduced to the cellular scale, enabling a wider treatment scale than ever before.

1.1.1 Nanoparticles and Nanotechnology

The nanoscale comprises materials of sizes under 100 nm. At these dimensions, the increase in surface area produces properties vastly different than those of the bulk counterpart due to quantum size effects. Nanomaterials are able to cross cell barriers and be selectively activated, and are currently being used in targeted drug delivery, enhancement of chemo and radiotherapies, magnetic particle imaging, and as contrast agents for magnetic resonance imaging (MRI).[3–9] There is especially interest in nanoparticles with high photothermal and colloidal stabilities for these applications.[10]

For biomedicine, nanotechnology is one of the fastest growing research areas. When particles have a single domain, they are able to absorb more radiofrequency to generate heat while leaving healthy surrounding cells unaffected. Thus, a superparamagnetic material is the optimal candidate for MH. It is important that the therapeutics have low toxicity and minimal nonspecific binding *in vivo*.

1.1.2 Magnetic Hyperthermia as an Oncology Treatment

An often-undesirable side-effect of applying an alternating current (AC) magnetic field to exothermic magnetic nanoparticles is the generation of heat. However, this property can be capitalized upon for thermotherapies.[11] Protein denaturation begins at 40 °C, and clinical applications of magnetic hyperthermia (MH) operate through the elevation of temperatures from 40-43 °C to induce apoptosis in malignant cells.[12–14]

MH has been combined with radiotherapy, chemotherapy, and magnetic particle imaging to enhance their cytotoxic effects via intratumoral injection of magnetic nanoparticles.[4,9,12,15–17] However, these approaches are limited by low heating efficiency, heterogenous outcomes, and

still require direct-injection of the nanoparticles, which prevents deep-tissue tumors from being reached.[3,18,19] These weaknesses can be mediated with the assistance of biologically targeted MH, which is a noninvasive treatment.[4]

MH localizes magnetic nanoparticles (MNPs) in tumor sites, where through the application of an AC magnetic field, converts electromagnetic energy to heat. MNPs can easily cross biological barriers to accumulate in the target cells, which enables extremely targeted treatment without causing damage to the healthy cells surrounding the tumor. Ideal modes of administration of the nanoparticles are either intravenous (IV) or through inhalation to target tumors inaccessible through direct injection, though both methods deliver lower concentrations to the tumor site. It is possible to optimize heat generation by tuning size, magnetic anisotropy, and saturation magnetization of the particles.[2,3,12,20–27]

Clinical use of MH remains limited. While MH has been reported as a promising tumor therapy, it has failed to heat damaged cells preferentially and effectively and research has not advanced enough to enable clinical use as a single modality treatment. Current reports mention difficulty in selectively accumulating particles that remain confined to the tumor site, and therapeutic effects have only been achieved at high MNP concentrations, field strengths, and frequencies that are often beyond tolerable limits in vivo. Literature reports fail to identify the specific properties required for an effective material, and no significant relationship has been found between synthetic method, material properties, and efficacy in vivo, where the influence of magnetic interactions remains unclear.[28]

Key parameters for an ideal MH material have been recognized as size, magnetic anisotropy, and saturation magnetization, but there is little understanding to how these values are influenced by physical and chemical properties of currently investigated materials. MH could be an incredible therapeutic technique for a variety of cancers, where the patient could feasibly be diagnosed and treated by a single modality. This work aims to elucidate the underlying mechanisms involved in developing a reasonable material for clinical applications of MH. there is a high demand for technology that enables homogenous delivery of heat within a clinically tolerable time frame that can also operate on a wider variety of tumors.

1.2 Material Requirements for Magnetic Hyperthermia

1.2.1 Magnetism

All materials possess some magnetic properties. Diamagnetism is a property of all matter, and from it stems all other types of magnetism. These relationships are depicted in Figure 1.1. Diamagnetic materials contain independently operations atoms that are weakly repelled by

magnetic fields and contain no unpaired electrons, and as such diamagnetism is observed only in purely diamagnetic materials.[29]

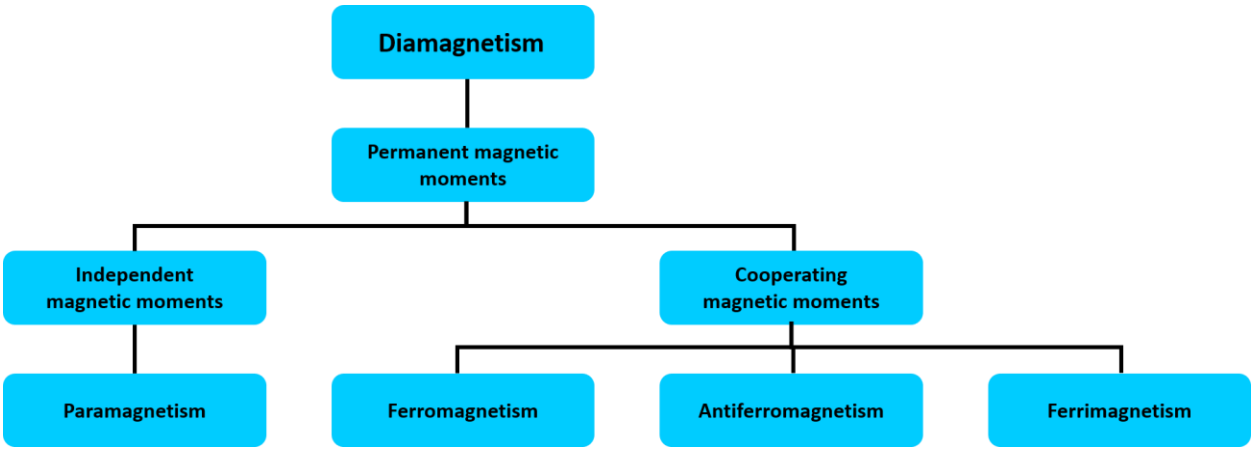

Figure 1.1. *Flowchart of the various types of magnetism.*

Every type of magnetism born from diamagnetism possesses a permanent magnetic moment. These permanent magnetic moments are then split into two categories: independent magnetic moments and cooperating magnetic moments. Paramagnetic materials have some number of unpaired electrons and are slightly attracted to magnetic fields. The independent magnetic moments experienced mean there is no order to the electron arrangement (Figure 1.2).[29] Application of an external magnetic field will produce some positive net magnetization.

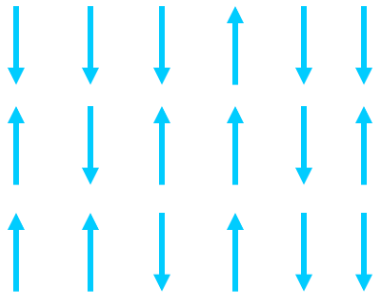

Figure 1.2. *Paramagnetic domain ordering.*

Ferromagnetic materials tend to experience spontaneous spin alignments parallel to each other, even in the absence of an applied field, enabling lower energies. All ferromagnetic materials have a Curie point, where at any temperature above this point the material loses its magnetic properties. Because of the lower energy, exceeding the Curie temperature results in greater

energy due to disorder overwhelming the ferromagnetic order. Some examples of ferromagnetic materials are iron, cobalt, nickel, their alloys, and alloys of some rare-earth metals.[30]

Ferromagnetic materials orient into magnetic domains with overall uniform alignment (Figure 1.3). The boundaries of these domains move to encompass the entire material when exposed to a magnetic field, where the removal of the field produces a permanent magnet and the material remains magnetized. If one domain grows to take over the entire material, saturation is achieved. If the material is heated to the Curie temperature and magnetic properties are lost, cooling back below this point will produce a spontaneous realignment of the domains.[30]

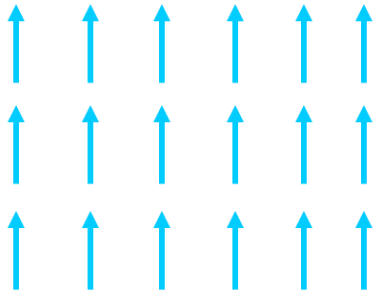

Figure 1.3. *Ferromagnetic domain ordering.*

Antiferromagnetic materials have domains that point in opposite directions (Figure 1.4). When all neighbors are antiparallel, the material is considered to be antiferromagnetic and possesses a net magnetic moment of zero. Antiferromagnetism is typically only observed at low temperatures.[30]

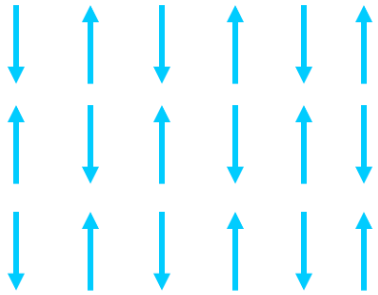

Figure 1.4. *Antiferromagnetic domain ordering.*

Ferrimagnetism is a form of cooperative magnetism that is similar to ferromagnetism in the sense that magnetism is retained after the removal of an external field, but similar to antiferromagnetism with the antiparallel ordering of electron spins. The magnitude of these magnetic moments is unequal (Figure 1.5).[30]

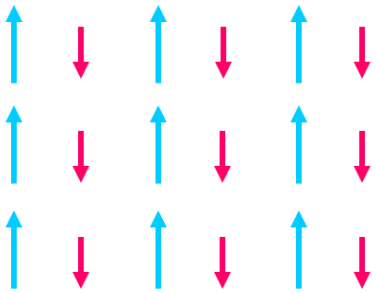

Figure 1.5. *Electron spin alignment for a ferrimagnetic material.*

At the nanoscale, both ferro and ferrimagnetic particles exhibit superparamagnetic behavior below a critical size, where magnetization flips randomly from temperature influence, referred to as Néel relaxation (eq. 1.1). These materials are additionally subject to Brownian motion. In the absence of a magnetic field, the net magnetization of the particles is zero; when an external magnetic field is applied, the particles magnetize much like paramagnets, but with a much larger magnetic susceptibility.

1.2.2 Heating Mechanisms and Figures of Merit

Nanoparticles, existing at sizes under 100 nm in diameter, are of widespread interest in biotechnology, electronics, and high frequency applications due to the novel properties exhibited relative to their bulk counterparts.[31] Decreasing particle size increases the surface to volume ratio of the particles, increasing the fraction of surface atoms available, which in turn increases the surface energy and reactivity of the particles.[32] With magnetic nanoparticles, the reduction in size produces permanent magnetic losses and a shift from the paramagnetic to the superparamagnetic regime, thereby increasing the magnetization per atom. Upon entering the nanoscale, magnetic particles can be ferromagnetic or superparamagnetic. At the nanoscale, multiple domains are energetically unfavorable, producing single domain nanoparticles.[33]

Figure 1.6 depicts the key differences between ferrimagnetic and superparamagnetic nanoscale materials. The ferrimagnetic particles (blue) contain multiple domains with at least one spin. Prior to the application of an external magnetic field, these spins are randomly oriented. Upon application of a magnetic field, all the spins align in a single direction, magnetizing the material. When the external field is removed, the material is demagnetized.

With superparamagnetic materials (pink, Figure 1.6), each particle contains only one domain. Similar to the ferrimagnetic particles, spins are randomly oriented until an external magnetic field is applied. This orients each spin in the same direction, and removal of the external magnetic field demagnetizes the material. For superparamagnetic materials, resultant magnetization is

enhanced relative to their multi-domain counter parts, as magnetization becomes a sum of the individual magnetic moments.

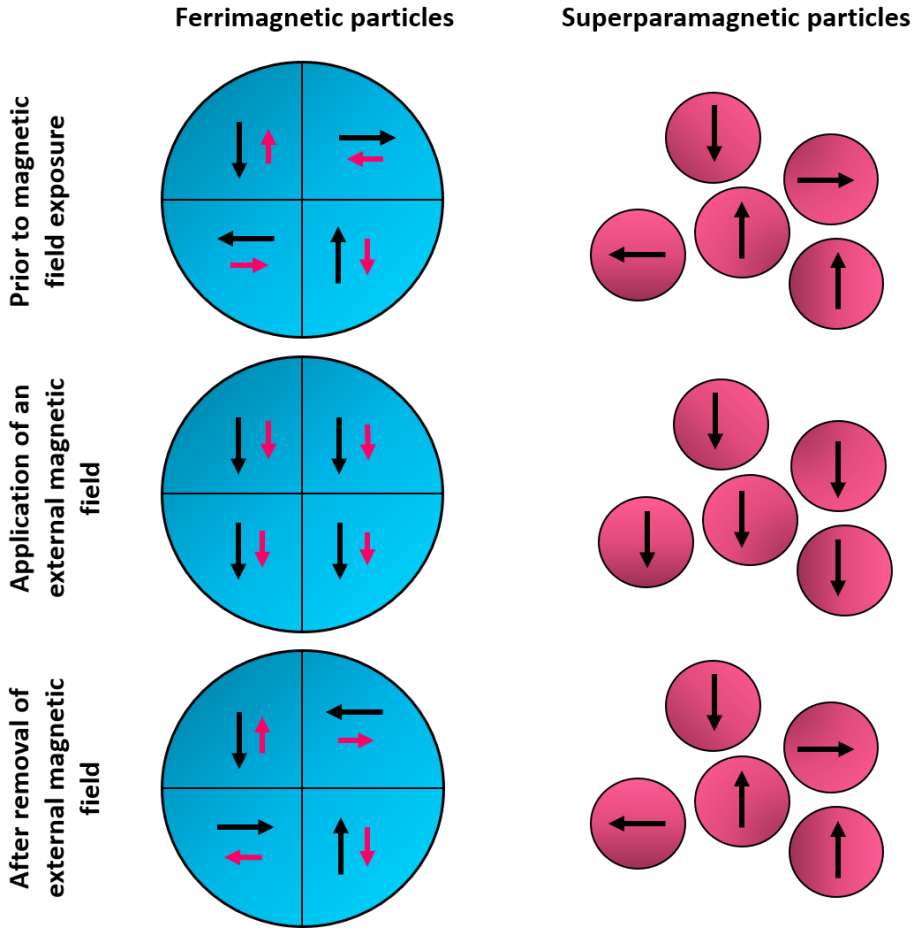

Figure 1.6. *Comparison of ferrimagnetic and superparamagnetic spin alignments in nanoparticles before, during, and after the application of an external magnetic field. The arrows depict the direction of spin orientation. Adapted from Belyanina et. al.*[10]

Magnetic heating is achieved through two primary mechanisms: hysteresis and relaxation. The primary method of heat formation in nanoparticles is hysteresis, where atomic spins are coupled to the crystal lattice.[24] Hysteresis is observed in materials with multiple magnetic domains, where an AC field continuously orients the particles in the direction of the applied field at several hundred kHz. This transfers electromagnetic energy to the lattice in the form of heat. Superparamagnetic materials have magnetic moments that spontaneously orient with thermal agitation and are not hindered by lattice orientation, therefore hysteresis is not observed.[34]

The two primary relaxation mechanisms involved in heat generation are Néel and Brownian. Because these motions are not impacted by deep-tissue location, they are suitable targets for MH.[16] Néel relaxation (τ_N) rapidly changes the magnetic moment of the particle when exposed to an alternating magnetic field. This is referred to as internal dynamics. The rapid realignment of spins is prohibited by the crystalline structure, and heat is generated by the resulting friction. This friction can be hindered by anisotropy.[21]

Néel relaxation is given by

$$\tau_N = \tau_0 e^{\frac{25T_B}{T}} \tag{1.1}$$

where T_B is the blocking temperature, T is the temperature, and τ_0 is the material-specific attempt time.[21] T_b defines the temperature at which a material exhibits superparamagnetic behavior. Below T_b, the material appears paramagnetic.

Brownian relaxation (τ_B) is frictional heat generated by the rotation of the particles as they attempt to realign with the changing field, known as external dynamics. An inhibition of Brownian relaxation has been observed in a cellular environment as a result of viscosity, which can counter the movement of particles and reduce the heat capacity.[3] Brownian relaxation can be mathematically represented as

$$\tau_B = \frac{3\eta V}{k_B T} \tag{1.2}$$

where V is the volume of the particle, k_B is the Boltzmann constant, and η is the viscosity.[21] For a finite system these processes take place together, and

$$\frac{1}{\tau} = \frac{1}{\tau_B} + \frac{1}{\tau_N} \tag{1.3}$$

where τ is the effective relaxation time.

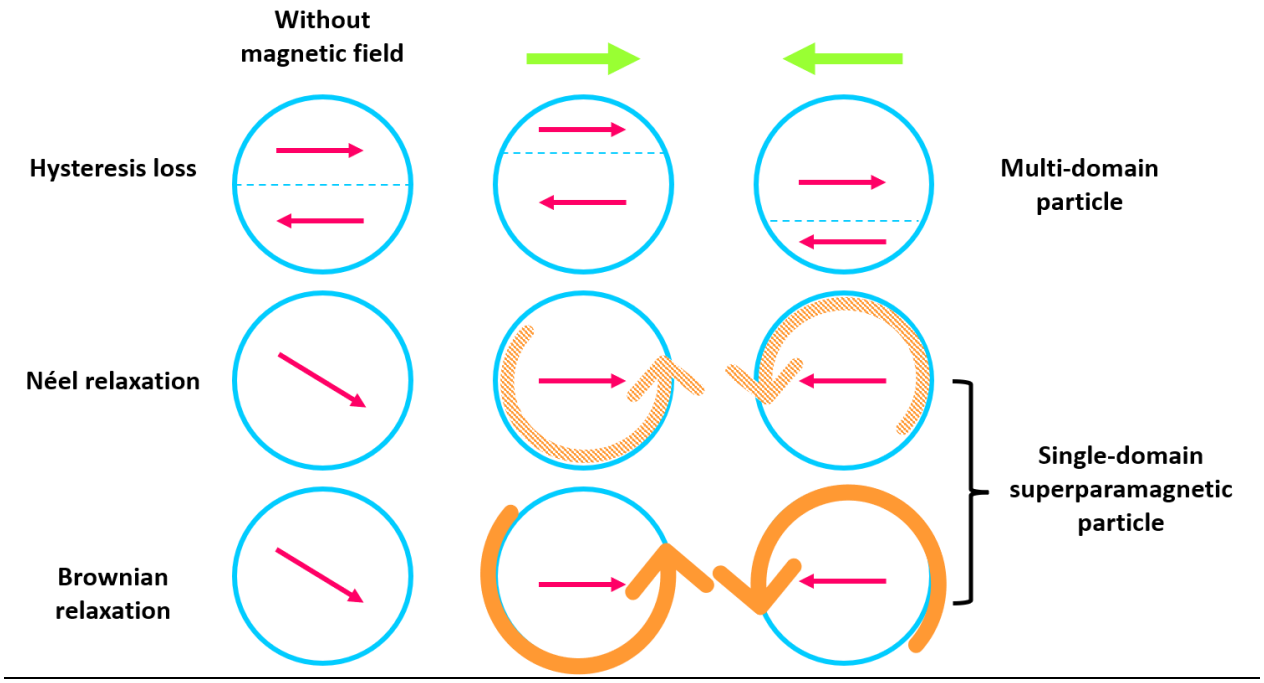

Figure 1.7. *Comparison of hysteretic losses, Néel relaxation, and Brownian relaxation for multi- and single domain nanoparticles in the presence and absence of an alternating magnetic field. The pink arrows inside of the circles represent spin direction, while the orange arrows on the outside of the circles represent the friction generated from the particle motions. Adapted from Chang et. al.*[12]

A comparison of Néel and Brownian mechanisms of heat generation compared to a multidomain particle are shown in Figure 1.7. A critical diameter D_c exists for MNPs, below which Néel relaxation dominates and above which Brownian relaxation dominates. D_c for magnetite is approximately 14 nm and 21 nm for maghemite.[35] The critical size for superparamagnetic MFO nanoparticles has been reported as 43 nm.[36] A particle size between 10 and 200 nm is necessary for MH applications; however, superparamagnetism is typically only observed below 50 nm.[37]

The most common parameter for heat generated is the specific absorption rate (SAR).[38] This is system-dependent and depends on strength *H* and frequency *f* of the applied field. SAR quantifies the heating efficiency of a material, and needs to be maximized at low particle concentrations for MH applications. Due to the variety of synthetic methods for obtaining MFO nanoparticles, and the variety of properties that each method offers, there are certain synthetic modifications that can be made to maximize the SAR.

SAR is written as

$$SAR = \frac{C}{m_{np}}\left(\frac{dT}{dt}\right) \tag{1.4}$$

where C is the heat capacity of the fluid, m_{NP} is the mass of the suspended magnetic phase, and dT/dt is the slope of the temperature rise T with respect to time t.[39] Experimentally, this is measured by suspending the material in liquid and subjecting it to an alternating magnetic field. The value of SAR depends on all parameters of the nanoparticle (i.e., size, shape, structure, saturation magnetization, susceptibility, H, f) and eq. 1.4 can be rewritten as

$$SAR = \frac{8\pi^3 \mu_0{}^2 M_S{}^2 r^3 H_0{}^2 f^2 \tau}{3\rho k_B T\left(1+2\pi f\tau\right)^2} \tag{1.5}$$

where μ_0 is the permeability of free space, H_0^2 is the magnetic field, ρ is the particle density, and M_S is the saturation magnetization. For an effective material for MH, biokinetics, biodistribution, and biodegradation must all be achieved while maintaining a high SAR.[21] For clinical applications, an optimal working frequency falls between 130 and 500 MHz and H_0 below 600 Oe.[40] SAR is often interchanged with the specific loss power (SLP), both of which have been found to increase with M_S.[26,35,41]

1.2.3 Manganese Ferrite as a Material Candidate

Iron-based nanoparticles have, at present, been the most frequently studied material for MH applications with both superparamagnetic iron oxide, Fe_3O_4, and maghemite, γ-Fe_2O_3, materials being extensively studied for their effectiveness in clinical settings, including activated drug delivery, and as MRI contrast and MH agents.[2,5,37,42–46] Introducing different dopants to Fe_3O_4 can improve heating performance and provide a range of electrical and magnetic properties that are influenced by the distribution of cations within the crystal lattice.[47] This is due to the antiparallel magnetic moments of tetrahedral and octahedral sites in the crystal lattice. Other divalent transition metals include Mn^{2+}, Mg^{2+}, Co^{2+}, Ni^{2+}, and Zn^{2+}. Additional considerations are the biocompatibility of the dopant used for applications to MH. A proposed alternative to Fe_3O_4 and γ-Fe_2O_3 is $MnFe_2O_4$ (MFO). MFO exhibits high permeability, M_S, resistivity, and chemical stability.[48] These properties make MFO a promising candidate for MRI and, by extension, MH.[17,21,49–51]

Ferrites belong to the spinel class. For a normal spinel, there are three atomic layers to the fcc arrangement, where the third layer is displaced from both the first and second, creating a series of holes that can be filled with ions. Figure 1.8 depicts a spinel ferrite unit cell, where the orange circles represent the ccp oxygen anions, the green circles represent the tetrahedral lattice sites, and the blue circles represent octahedral sites. A spinel ferrite unit cell contains 32 oxygen

anions, 64 tetrahedral sites, and 32 octahedral vacancies.[52] The geometries of the holes are dictated by how many ions they can be coordinated to, with two tetrahedral holes and one octahedral hole per atom created by the cubic closest packing (ccp) oxygen anions.[53] Most ferrites are ferrimagnetic, including MFO.

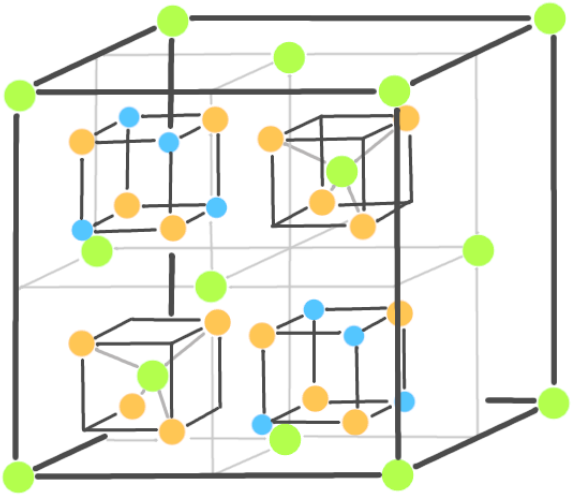

Figure 1.8. *The lattice arrangement of a spinel ferrite. Orange circles represent ccp oxygen anions, green circles represent tetrahedral lattice sites, and blue circles represent octahedral lattice sites. The rear four units have been omitted for clarity.*

MFO crystallizes as a mixed spinel, where both normal and inverse structures can be observed. Chemical composition produces profound effects on the magnetic properties of spinel ferrites, most notably from the divalent cations.[52] The general formula for a MFO spinel ferrite is

(1.6)

where the parentheses represent the tetrahedral occupancy of the material, brackets represent the octahedral location, and *x* represents the degree of inversion of cations among tetrahedral and octahedral sites. For a normal spinel arrangement, *x* is equal to 0, and for an inverse spinel *x* would have a value of 1. Therefore, the degree of inversion for any spinel crystal can vary between 0 and 1, and the range becomes broader as the particle size decreases.[54] Magnetic properties are closely related to inversion degree, which can be influenced by cation radii and energy preferences of tetrahedral and octahedral lattice sites.[55]

Figure 1.8 depicts a spinel structure, where the green circles depict tetrahedral holes and the blue circles represent octahedral ones. Fe_3O_4 exhibits an inverse spinel structure, where all A cations and ½ of all B cations occupy octahedral sites, and the remaining ½ of B cations occupy the tetrahedral sites. Unlike Fe_3O_4, MFO has zero crystal field stabilization energy (CFSE), and the divalent cations have no preference for tetrahedral or octahedral sites, resulting in a mixed spinel

arrangement. Mn^{2+} is high-spin in tetrahedral lattice sites and intermediate-spin in octahedral ones, greatly influencing magnetic properties.[56] The ionic radii of Mn^{2+} and Fe^{3+} are relatively similar, resulting in little preference for either lattice site, where smaller cations would typically prefer the site of lower coordination.

The magnetic properties of spinel ferrites are the result of ions with different valences in the crystal structure, where the ccp oxygen anions are surrounded by a combination of divalent and trivalent cations.[57] The unpaired ions create parallel but oppositely aligned magnetic moments. Because there is no cancellation of moments, the particles can be spontaneously magnetized. Resultant magnetism is dependent on how the unpaired spins of metal ions are coupled, with the strongest coupling occurring between ions on neighboring tetrahedral and octahedral sites. The higher the number of unpaired *d*-electrons, the greater the spin-only magnetic moment. Mn has five unpaired electrons, owing to its high spin number. With higher magnetization than Fe_3O_4, MFO also exhibits reduced magnetocrystalline anisotropy.

The SAR of nanoparticles is dependent on a multitude of factors: synthetic method, particle size distribution, and degree of crystallinity. Because of this, it is difficult to optimize for size when there are compounding independent variables at play. SAR is commonly reported as a function of particle diameter.[58] Figure 1.9 offers a comparison of SAR values for the two most competitive MH candidates: Fe_3O_4 and $MnFe_2O_4$. Synthetic method was not consistent among references. Particle size is given, in nm, on the *x*-axis, and SAR, given in W g^{-1}, is shown on the *y*-axis.

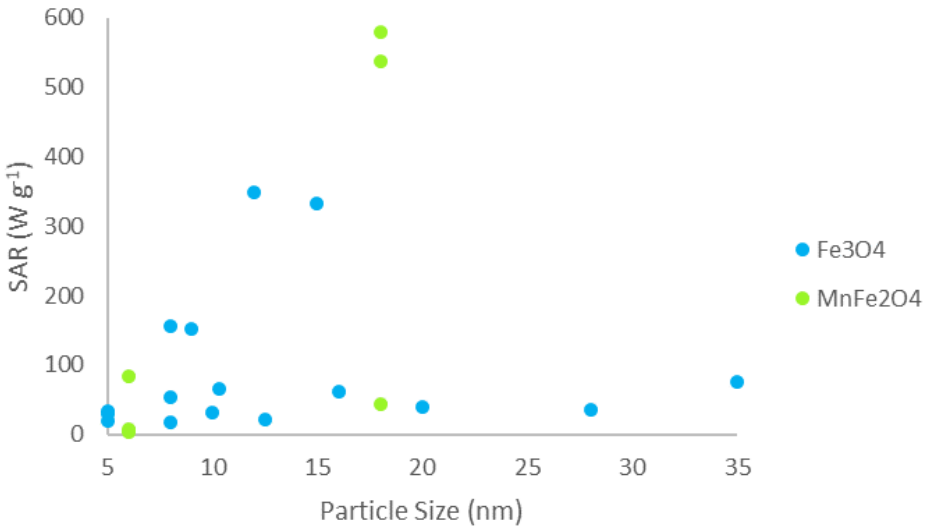

Figure 1.9. *Selected values from the literature comparing particle size (nm) to SAR (W g^{-1}) for Fe_3O_4 and $MnFe_2O_4$ nanoparticles.*[5,11,21,59–65]

As can be seen in Figure 1.9, there is no obvious correlation between particle size and SAR for either material. Additionally, it should be noted that some of the smaller-sized particles produce larger SAR values than their larger counterparts. This brings attention to the fact that the correlation between particle size and SAR typically only holds up for samples synthesized under identical conditions, and highlights the variance in material properties that can be offered by synthetic condition. Additional propositions for increasing SAR include tailoring the nanoparticle shape, though this introduces toxicity *in vivo*.[18]

1.3 Objectives

At present, particle size is most often reported as the controlling factor in optimizing the magnetic properties of a material for maximizing heat generation.[66] Nanostructure design is incredibly important in functionalizing materials, and understanding key parameters is critical to better target magnetism.[67] Efficient heating for MH is dependent on concentration, stability, frequency, and field strength. Magnetic behavior should be superparamagnetic and heating must be achieved under low magnetic field, as it is essential to reach an appropriate temperature in reasonable time (<10 min).[68]

An idealized material for MH will have higher heating efficiency than what is currently reported that can be achieved within a clinically tolerable range. There is a lack in consistency and mechanistic understanding regarding how best to tailor material properties to maximize SAR, and little agreement in how to optimize the multitude of factors that contribute to variation in material properties. This work aims to improve understanding of material contributions and build a comprehensive model for MH applications. Through the use of multivariate data analysis, it will be possible to identify how to synthetically optimize for M_S, an important component of SAR.

Chapter 2. Synthesis and Characterization of Manganese Ferrite Nanoparticles

2.1 Synthesis

Synthesis at the nanoscale unlocks material properties that are strongly dependent on size and shape. As particle size decreases, the demand for consistent and homogeneous preparation of nanoparticles increases. Several synthetic approaches exist to produce nanoparticles, though they are often difficult and require expensive materials. A principal concern in nanoparticle synthesis is the rigorous control required, where every step must be closely monitored to ensure uniform product size and composition.

2.1.1 Nanoparticle Synthesis

The properties of spinel ferrites are strongly dependent on synthetic technique. Synthetic approaches for MFO nanoparticles include reverse-micelles, sol-gel, ligand-exchange, hydrothermal, solvothermal, borohydride reduction, polyol, and co-precipitation, each of which offer different degrees of control over material properties.[48,52,68,69] Co-precipitation is the most popular choice for a scalable synthesis but offers poor control over particle size and shape, in addition to forming products with low saturation magnetizations due to agglomeration and polydispersity, and thus is not an appropriate choice for nanoscale fabrication.[70] The thermal decomposition of metal complexes is the method of choice for nanoparticle synthesis due to ease of preparation, affordability, and production of a highly crystalline, monodisperse, and stable nanoparticles.

There are two main types of nanoparticle synthesis: top-down and bottom-up.[71] The top-down approach involves breaking down a metal into the desired size, while bottom-up decomposes a precursor before nucleation and growth into particles. Nanoparticle synthesis in solution relies on two components: nucleation and growth. When precursors react in solution, stable nuclei are formed, enabling growth. The major barrier of precipitation reactions is poor control over particle size as the only methods of growth control are kinetic (temperature, pH, stir rate, concentration).[69]

Crystals cannot form until the solution reaches supersaturation, which is accomplished when the free energy of the precipitating species exceeds the minimum energy concentration and provides a site for nucleation to occur. Quick nucleation, both to commence and complete a reaction, produces high homogeneity of product, thus growth must begin synchronously and proceed under the same conditions to achieve a uniform size distribution. High crystallinity is absolutely

essential to maximize material functionality.[72–74] This work utilizes a bottom-up approach to maximize control over growth conditions through a variety of synthetic modifications.

2.1.2 Reproducible synthesis of MFO nanoparticles

A facile polyol route, adapted from Günay *et al.,* with modifications, was employed in the synthesis of $MnFe_2O_4$ nanoparticles.[75] Manganese (II) acetate tetrahydrate, 1 mmol, and iron (III) acetylacetonate, 2 mmol, were covered with tetraethylene glycol (TEG) and stirred under N_2 blanket. A two-step heating process was used, where the temperature was held constant at 240 °C for two hours to allow for decomposition of the precursors and then raised to 282 °C for an additional hour, enabling growth of the nanoparticles. The resulting dark brown solution was cooled naturally or in stepwise reductions before washing in a 1:1 mixture of ethanol and deionized water. After three washes, the black precipitate was separated from the solution by magnet and dried at 100 °C.

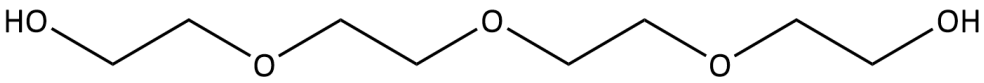

Figure 2.1. *Chemical structure of tetraethylene glycol.*

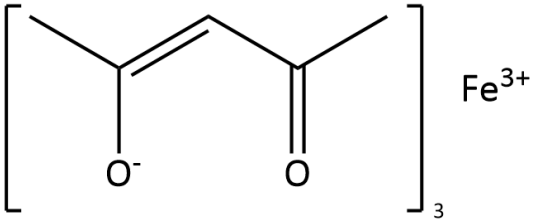

Figure 2.2. *Chemical structure of iron (III) acetylacetonate.*

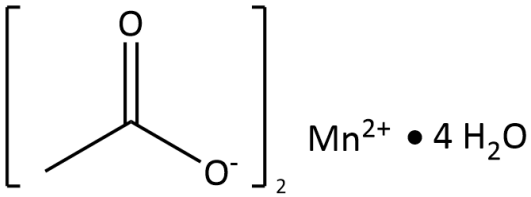

Figure 2.3. *Chemical structure of manganese (II) acetate tetrahydrate.*

The exact mechanism of MFO synthesis by thermal decomposition is unknown, but it loosely involves the reduction of organometallic salt precursors followed by an oxidation. Chemical structures for all precursors are shown in Figures 2.1-2.3, with a depiction of a TEG encapsulated nanoparticle in Figure 2.4. This surface coating imparts biocompatibility upon the nanoparticles, though this comes with the caveat of impacting magnetic properties. This effect will be discussed more in later chapters.

It is possible to achieve a narrow size distribution and enhanced magnetic properties with the use of TEG as a chelating agent for several reasons. First, TEG is reductive at high temperatures, allowing for the instantaneous reduction of metal cations to nanoparticles. High boiling solvents improve crystallinity by clearly separating nucleation and growth.[76] This minimizes agglomeration while encouraging a narrow size distribution of spherical particles by preventing inhomogenous growth at nucleation. A sufficient amount of exterior coating is essential for *in vivo* applications, as suspension in biological media may remove some of the shell.[77] Additionally, functionalized surfaces have been shown to possess high specificity for tumor cells.[78]

In this synthesis, TEG acts as both solvent and surfactant, leaving the product suspended in water-soluble medium, resulting in no dependence of solute concentration on particle size. Because of this, a high solid content is achieved without the use of additional stabilizers.[79,80] Additionally, thermal decomposition in the organic phase may improve magnetic sensitivity.[81,82] This particular synthesis offered spherical nanoparticles, which are ideal for homogeneous temperature distribution.[58,83]

There are a variety of synthetic options for surface-functionalized nanoparticles. Polar surfaces are energetically unfavorable and thus a surfactant is used to passivate the surface. Coating the MFO particles in TEG maintains biocompatibility and prevents oxidation, essential components for applications *in vivo*. The motions discussed in eq 1.1 and eq. 1.2 can be hindered in physiological environments, and so nanoparticles should be coated with a water-soluble material to prevent heat losses.[21]

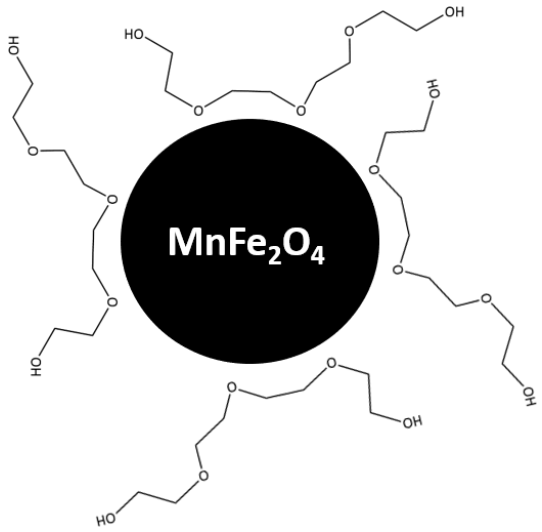

Figure 2.4. *Depiction of one TEG coated nanoparticle.*

2.2 Characterization Techniques

Multiple characterization techniques were used to parameterize all features of the synthesized nanoparticles to encompass physical, chemical, and magnetic properties. Selected methods were limited to those that enabled frequent quantification for ease of modeling, which will be presented in chapter 4. All characterization techniques utilized are outlined in Table 2.1, along with a brief description of the purpose of each.

Table 2.1. *Characterization Techniques Employed*

Technique	Purpose
Powder X-Ray Diffraction (XRD)	Crystallite size Lattice Parameter Microstrain Phase determination
Laser Ablation Inductively Coupled Mass Spectrometry (LA-ICP-MS)	Cation occupancy Elemental composition Sample homogeneity
Vibrating Sample Magnetometry (VSM)	Magnetic Properties
Thermogravimetric Analysis (TGA)	Quantification of coating Thermal stability
Transmission Electron Microscopy (TEM)	Particle size Particle visualization
Fourier Transform Infrared Spectroscopy (FT-IR)	Bonding Cation occupancy

2.2.1 X-Ray Diffraction

A crystal is composed of distinct and parallel planes separated by defined distances. Powder X-Ray Diffraction (XRD) uses the diffraction patterns of incident X-rays to structurally characterize crystalline substances. This enables the user to obtain an impressive amount of information regarding the crystal structure of the sample, including phase determination, crystallite size, lattice parameter, microstrain, bond angles, etc. A focused X-ray beam is either reflected off the crystal surface or diffracted by the atoms of the crystal lattice, producing characteristic patterns that can be further quantified.[84]

Diffraction occurs in accordance with Bragg's law

$$n\lambda = 2d\sin(\theta) \tag{2.1}$$

where n is the diffraction order (n=1 is first order, n=2 is second order, and so on), λ is the radiation wavelength, d is the interatomic distance, and θ is the angle of incidence. Equation 2.1 defines the relationship between wavelength and scattering angle, and is the basis for how crystalline materials can produce characteristic peaks when exposed to X-rays of specific wavelengths. When reflections are constructive, producing a phase shift of any multiple of 2π, eq 2.1 is satisfactory. Diffraction patterns offer many pieces of information about a material. The position of the peak corresponds to the unit cell size and shape, the intensity of the peak corresponds to the position and atomic number of the atoms composing the unit cell, and the width of the peak is influenced by structural properties. A wider peak indicates a smaller crystal.

For this work, a Malvern Panalytical X'Pert Pro MPD diffractometer with CuKα radiation (λ=1.5406 Å), $20° \leq 2\theta \geq 90°$, 45 kV and 40 mA, was used to collect diffraction patterns, and X'Pert HighScore Plus software was used to determine crystallite phase, size, lattice parameter, and microstrain through Reitveld refinement. All patterns were matched to the PDF-2 pattern for $MnFe_2O_4$ (JCPDS card no. 01-074-2403). Samples were all assigned to the Fd3m space group.

Scherrer analysis was employed to determine the average crystallite size for each sample. The Scherrer equation

$$\tau = \frac{K\lambda}{\beta\cos(\theta)} \tag{2. 2}$$

gives the relationship between mean crystallite size, τ, and line broadening of the diffraction pattern at the full width at half maximum (FWHM), denoted β. The shape factor, K, is dimensionless and varies with the crystallite shape, and θ is the Bragg angle. Use of eq 2.2 is limited to nanoscale crystallites. The FWHM can be influenced by factors such as imperfections in the crystal lattice and sample inhomogeneity, which can shift the peaks and change their shapes. The influence of all of the variables in eq 2.2 tend to produce crystallite size calculations that are larger than the actual crystal. For this work, all calculations were completed with X'Pert HighScore Plus software.

The most notable diffraction peaks are indexed according to plane, labeled in Figure 2.6. To serve as a reference for experimental XRD patterns, Figure 2.6 can be converted to a stick pattern of relative intensities of characteristic peaks. This stick pattern is shown in Figure 2.7, and was used as the reference for all XRD patterns in this work.

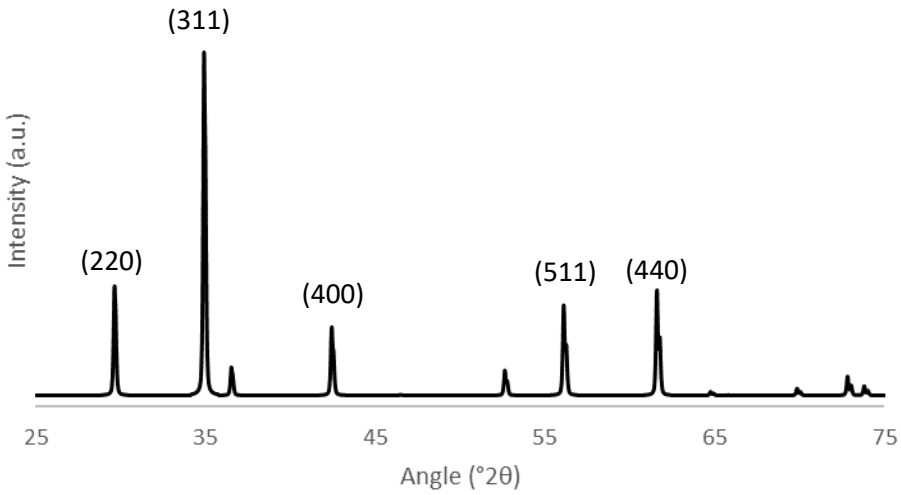

Figure 2.6. *Simulated XRD pattern for $MnFe_2O_4$. Peaks are indexed according to plane.*

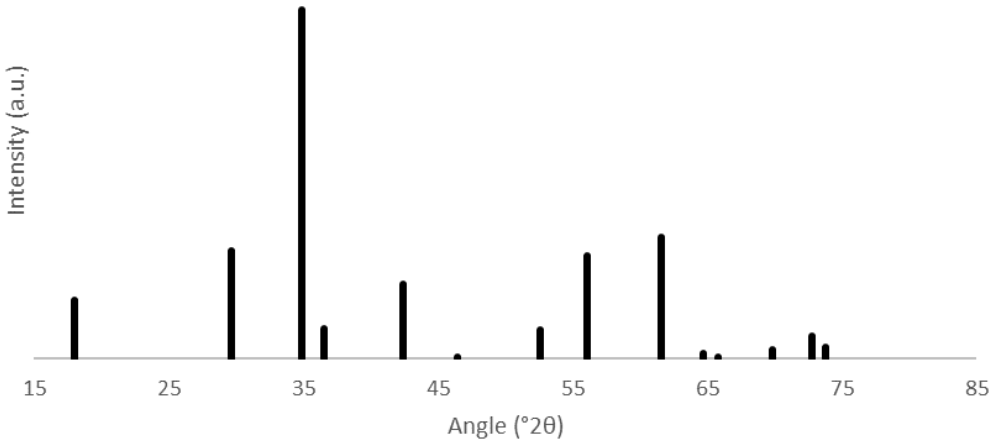

Figure 2.7. *Stick pattern for $MnFe_2O_4$, JCPDS reference code 01-074-2403. This pattern provides the reference set for all XRD measurements in this work.*

Reitveld refinement enables reasonable quantification of additional details such as lattice parameter and microstrain by performing a least-squares refinement of curve fitting to minimize the difference between the observed and calculated XRD patterns.[85] Lattice parameter determines the reflection position, while microstrain is the root mean square of all lattice parameters for the sample.

2.2.2 Laser Ablation Inductively Coupled Mass Spectrometry

Laser ablation inductively coupled mass spectrometry (LA-ICP-MS) provides elemental, but not structural information, on a solid. A laser beam is focused on the sample, which is ablated before being transferred to a secondary ionization source. Vaporized particles are transferred out of the chamber by a carrier gas, atomized, ionized until they form ions. The product is then suitable for analysis by mass spectrometer.[86]

The Mn to Fe ratio for each sample was verified as 1:2 using an Agilent ICP-MS. Powder samples were pressed under 3 tons into 13 mm pellets and a scan speed of 50 µm sec^{-1} with 4 J cm^{-2} fluence was used to collect 1.5 mm lines. External standards were used for comparison.

2.2.3 Vibrating Sample Magnetometry

Vibrating sample magnetometry (VSM) is used to quantify the magnetic properties of a material. The application of an external magnetic field *H* aligns the magnetic moments of the nanoparticles with the applied field, resulting in a net magnetization of the particles. This results in a reversible, S-shaped function. The sample is placed in a constant magnetic field, which it will align with. The sample moves up and down, and the magnetic dipole moment of the sample creates a magnetic field that changes as a function of time. This alternating magnetic field induces an electric field in the pickup coils of the VSM, which is proportional to the magnetization of the sample.

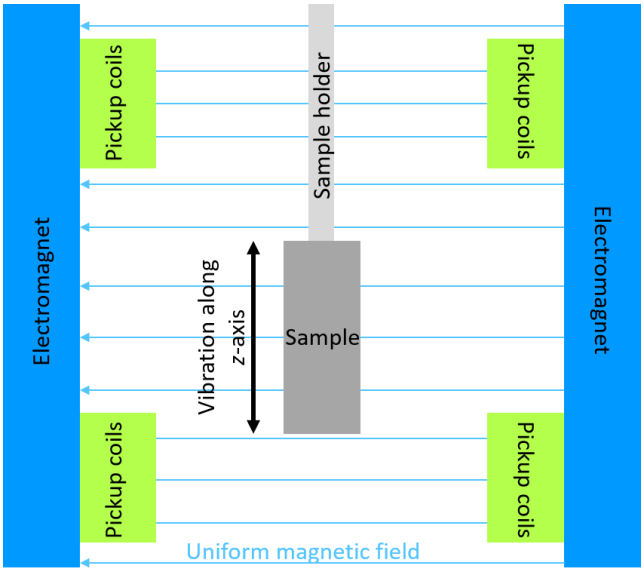

Figure 2.8. *Schematic of a VSM sample chamber.*

Magnetics measurements were obtained on powder samples with a Quantum Design DynaCool physical property measurement system (PPMS) outfitted with a D525 vibrating sample magnetometer (VSM). Unless otherwise noted, measurements were taken in a field ranging from

-2 to 2 T at 300 K. Zero-field cooled (ZFC) and field cooled (FC) measurements were obtained at 100 Oe.

2.2.4 Thermal Gravimetric Analysis

Thermal gravimetric analysis (TGA) is a technique used to measure the thermal stability of a material. Weight is measured over time as a function of temperature. This provides physical properties of the sample, including phase transitions, adsorption, desorption, absorption, as well as chemical properties, such as thermal decomposition, chemisorptions, and solid-gas reactions. The TGA curve displays either temperature or time on the *x*-axis with mass on the *y*-axis. The first derivative of this curve provides inflection points useful for more detailed analysis.[87] Dynamic thermogravimetry, which will be the focus of TGA measurements for this work, involves the linear application of heat to the sample.

For a thermally stable sample, mass will not change for a given temperature range. Changes in mass appear as a stepwise function, where discrete intervals can be identified and attributed to sample properties. All thermal analyses were conducted on a TA Q5000 TGA to quantify the amount of TEG coating around the nanoparticles. Power samples were heated at 10 °C min^{-1} to 525 °C under an N_2 flow rate of 10 mL min^{-1}.

2.2.5 Transmission Electron Microscopy

A TEM consists of a column filled with a number of components: electron gun, magnetic lenses and apertures, cameras, and detectors. To form an image, electron beams are focused on a solid sample. The interactions of these electrons with the particles comprising the sample create an image that is focused on a screen. The electron beam is generated by a field emission gun (FEG), which can either be warm or cold. A cold FEG provides higher energy resolution than a warm one, as electrons are tunneled with an anode plate without causing any temperature increases.[88]

Transmission electron microscopy (TEM) offers the greatest spatial resolution of any of the techniques utilized in this work. This form of imaging enables structural and compositional details well within the nanometer range. In this work, TEM was employed to determine particle sizes and features. Images were collected on a JEM-F200 cold FEG electron microscope. Particles were suspended on a grid and imaged at 20x magnification. Particle size distributions were determined with ImageJ software, where diameters of at least 30 individual particles were plotted on a histogram to show the total size distribution.

2.2.6 Fourier Transform Infrared Spectroscopy

Fourier transform infrared spectroscopy (FT-IR) measures the absorption of a material. A beam of various frequencies of light is shown onto a solid sample, and the amount of that light that is

absorbed is measured. This is continued at various other frequency combinations and the data is converted to a spectrum via Fourier transform.[89]

FT-IR was used in this work to approximate Mn^{2+} content in octahedral sites. A Thermo Scientific Nicolet iS50 FT-IR with a Solid Substrate Far-IR filter was used to collect spectra down to 250 cm^{-1}. Silver bromide is transparent in the far-IR region and was used to create pellets for analysis. A 9:1 ratio of AgBr to powder sample was used to create 13 mm pellets under 3 tons of pressure. For all spectra, a background spectrum was taken to minimize CO_2 and H_2O signals, and a pure AgBr spectrum was subtracted from each sample. Absorbance was normalized to the maximum of v_2 to account for differences in pellet thickness.

Due to the mixed spinel crystal structure of MFO, quantification of site occupancies is necessary to better understand material properties. Cation distribution changes with the strength of superexchange interactions across tetrahedral and octahedral sites, which can be influenced by synthetic procedure.[60] Extended x-ray absorption fine structure (EXAFS) is a reliable method for determining cation occupancies but is prohibitive to daily analysis due to the requirement of a synchrotron radiation source. However, a linear relationship was found to exist between EXAFS determined cation distributions and the characteristic Fourier transform infrared spectroscopy (FT-IR) absorption bands of manganese-zinc ferrites.[90] These absorption bands are found in the far-IR range between 300 and 600 cm^{-1}.

Two absorption regions were of interest in this work, being above and below 480 cm^{-1}. The characteristic peak v_1 shifts in accordance with the percentage of cations occupying octahedral sites, located above 480 cm^{-1}, is the result of both Mn^{2+}-$Fe^{2+/3+}$ stretching and Mn^{2+}-O stretching, where the shift can be correlated to the amount of Mn^{2+} present. v_2 is related to the Fe^{3+}-O stretch, and v_3 is the Mn^{2+}/Fe^{2+}-O stretch. The model suggested by Shultz et. al.[90] proposes the equation for the determination of Mn^{2+} occupied by octahedral sites as

$$y = 0.0072x - 3.8343 \qquad (2.3)$$

where x is the wavenumber of the respective v_1 peak absorbance and y is the percentage of Mn^{2+} present in octahedral sites.

Chapter 3: Synthetic modifications and cation arrangements

3.1 Synthetic modifications

A number of synthetic conditions with organic salts have been shown to impact the meso and macrostructures of materials.[91] A variety of synthetic variations were introduced in an attempt to influence crystallite structure, crystallite size, and to alter cation occupancies within the crystal. All parameter boundaries were defined by reasonable limits for the confines of the synthesis, and only variables that could be directly controlled through synthetic modifications were considered.

Nanoparticles were synthesized under various concentrations, stir speeds, and cooling rates to produce a total of 23 samples, with all set points outlined in Table 3.1. [Fe] relates to the quantity, in mmol, of iron (III) acetylacetonate used in accordance with the defined 1:2 ratio of Mn to Fe precursor. Stir rate is the set point used for magnetic stirring during the synthesis, and dwell time refers to the amount of time at the conclusion of the synthesis that the reaction vessel was cooled at discrete intervals rather than performing an abrupt removal of the reaction vessel from the heat source.

Table 3.1. *Selected Synthetic Variables with Specific Set Points*

Synthetic variable	Set points
[Fe] (mmol)	1, 2, 4, 8
Solvent volume (mL)	20, 50, 80, 100
Stir rate (rpm)	200, 500, 900, 1200
Dwell time (min)	0, 90, 120, 150

Magnetic properties are also dependent on surface structure.[92] A magnetically dead layer, referred to as the Griffiths phase (GP), is the result of lattice disorder at the particle surface often due to phase inhomogeneity.[93] Depicted in Figure 3.1, the GP consists either of vacant lattice sites or zero-spin atoms, and can be a product of variations in synthetic parameters.[94] A variety of systems can experience behavior analogous to a GP, where random cation distributions increase the propensity for GP formation, with increased surface anisotropy occurring with decreasing particle sizes. While surface structure was not the primary focus of this work, the effect of the surface coating will be examined in the following sections.

Table 3.2. *Sample Naming Conventions for Synthetic Variations*

Sample ID	[Fe] (mmol)	TEG (mL)	Stir rate (rpm)	Dwell time (min)
S1	8	100	500	0
S2	4	100	500	0
S3	2	100	500	0
S4	8	80	500	0
S5	4	80	500	0
S6	2	80	500	0
S7	1	80	500	0
S8	8	50	900	0
S9	4	50	900	0
S10	2	50	900	0
S11	1	50	900	0
S12	4	20	900	0
S13	2	20	900	0
S14	1	20	900	0
S15	2	20	500	90
S16	2	20	500	120
S17	2	20	500	150
S18	2	20	500	90
S19	2	20	500	120
S20	2	20	500	150
S21	2	20	900	90
S22	2	20	900	120
S23	2	20	900	150

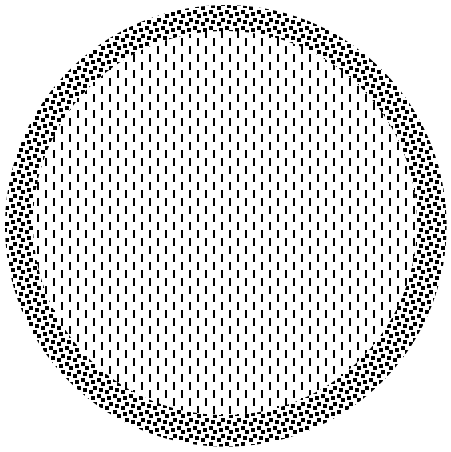

Figure 3.1. *Depiction of a Griffiths phase on a single particle, where the outer shell is disordered and the core particle is magnetically ordered.*

Each synthetic modification outlined in Table 3.1 will be discussed in the following sections, along with a summary of characterization techniques employed (XRD, TGA, and FT-IR) to study the effect of each modification on resultant material properties. Naming conventions for each sample are defined in Table 3.2, along with the respective synthetic variables. Quantifications from all characterization methods are summarized at the conclusion of section 3.1.3.

3.1.1 Controlled Cooling

Natural cooling of a reaction vessel does not allow for precise control over the particle growth process, often resulting in poor quality crystals with inhomogeneous size distributions. This is the result of supersaturation being pushed past its metastable limit, increasing the quantity of nuclei in solution. Quenching the solution from boiling halts nucleation and subsequent growth. Three methods of cooling were initially attempted to control particle size: natural, quenching from boiling, and an intermediate of the two. No appreciable change in particle size was obtained through any of the methods, necessitating further control over the particle growth mechanism.

Because cation arrangement can change based on the conditions at crystal formation, it was desired to better understand the influence of nucleation temperature on the cation distribution within the crystal lattice. Many methods exist for controlling particle size via thermal decomposition, including increasing the concentration of the iron precursor, altering the pH of the solution, and decreasing reaction temperatures. These methods do not enable precise control over size and none address the underlying mechanisms and time dependencies involved with nucleation and growth. A balance must be achieved between maximizing desired properties while producing particles of an optimal biocompatible size within the superparamagnetic regime.

Programmed cooling maintains the level of supersaturation within the metastable limit to minimize the appearance of new nuclei and increase the final particle size relative to natural cooling.[95] For this synthesis, a proportional integral derivative (PID) controller was used to maintain precise control over the cooling process. The controller maintained the temperature of the reaction flask for the duration of the synthesis in an attempt to prevent additional nucleation while promoting homogenous crystal growth.

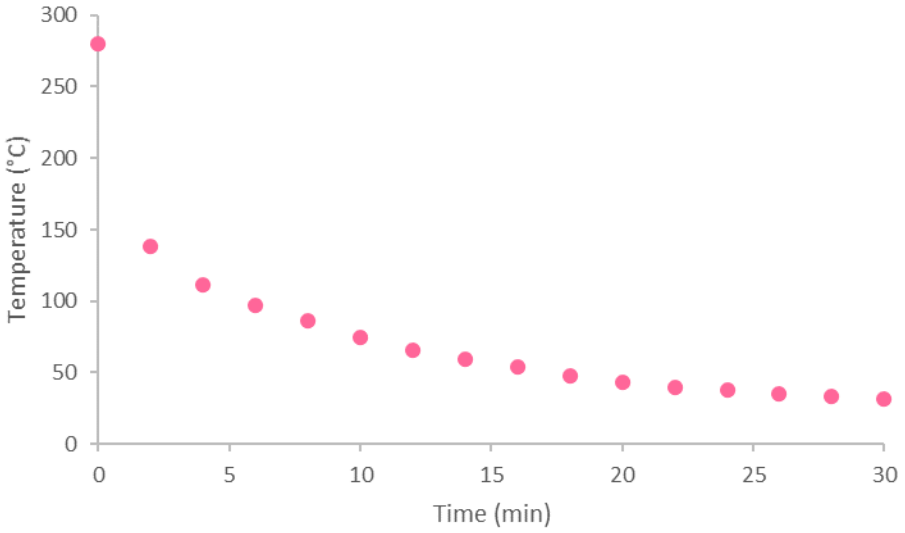

Figure 3.2. *Cooling curve for a naturally cooled sample.*

The cooling curve outlined in Figure 3.2, with time in minutes on the *x*-axis and temperature in Celsius on the on the *y*-axis, depicts the ambient cooling experienced by the reaction flask at the conclusion of the synthesis after the sample had been removed from the heat source. The sharpest temperature change, more than 100 °C, occurs between 0 and 2 minutes, wherein the greatest difference exists between the mixture temperature and its surrounding environment. During this time period, supersaturation is maximized. PID cooling was employed in an attempt to enable constant supersaturation through the entire cooling process, establishing greater user control over the growth mechanism to produce a tunable size distribution of MFO particles.

Figure 3.3, with time in minutes on the *x*-axis and temperature in Celsius on the *y*-axis, displays cooling curves for three dwell times: 90, 120, and 150 minutes. By establishing a controlled cool time, it was possible to eliminate the sharp temperature drop in the first two minutes of cooling exhibited in Figure 3.2. From prior experimentation with quenching the solution immediately after removal from the heat source, it was determined that cooling beyond approximately 50 °C was not influential in particle growth, and thus was omitted in the longer trials (120, 150 minutes). Relative to Figure 3.2, cooling is extended from a less than 20-minute period to a maximum of 150 minutes.

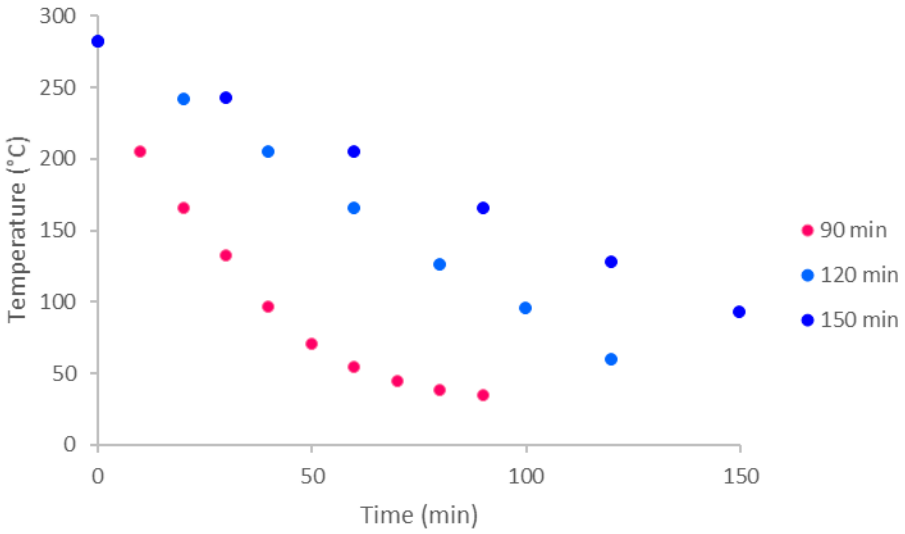

Figure 3.3. *Cooling curves for samples synthesized with a PID-controlled dwell of 90, 120, and 150 minutes.*

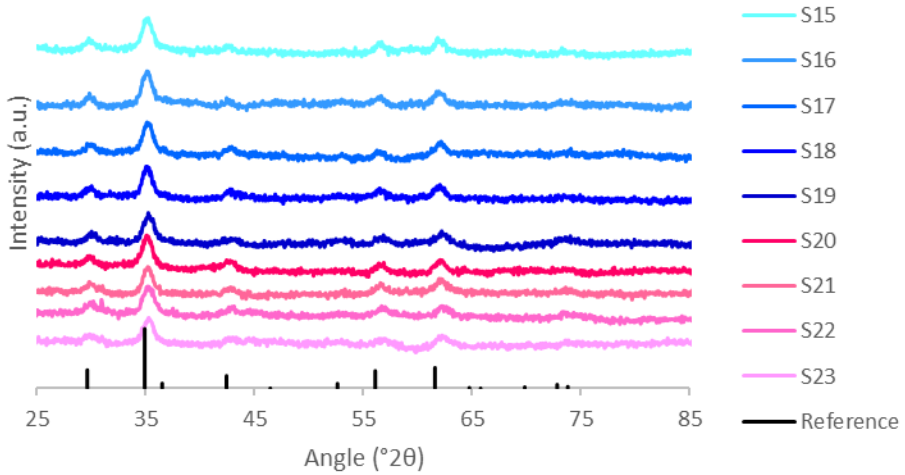

Figure 3.4. *XRD patterns for all samples synthesized with a dwell. Offset added for clarity.*

XRD characterization, in Figure 3.4, shows little difference between individual patterns. The characteristic peak of ferrites is seen at similar intensities around the diffraction angle 34 °2θ and aligns closely with the reference stick pattern (black lines). As such, it was determined that the addition of a dwell had no impact on the crystallinity of the MFO samples. Crystallite sizes ranged

from 7.5 to 11.7 nm, and lattice parameter varied between 8.41 to 8.48 Å with a maximum microstrain of 1.49%.

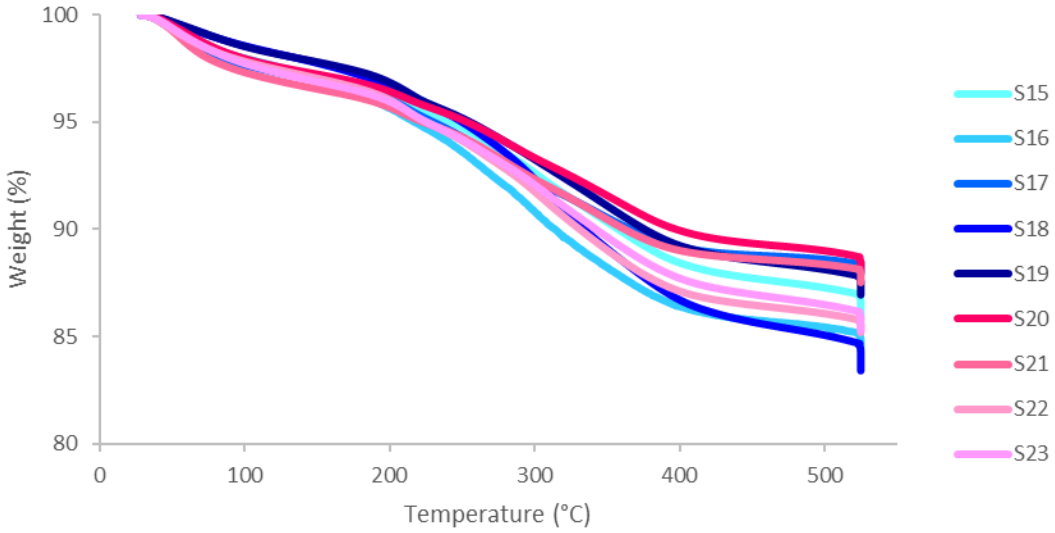

Figure 3.5. *Overlaid thermograms for all samples synthesized with a dwell.*

Thermal analysis, shown in Figure 3.5, was utilized to confirm the presence of TEG coating on the synthesized particles. Thermograms showed two distinct points of weight loss, where that occurring before 150 °C can be attributed to adsorbed water and the steeper decline after 200 °C is generally attributed to the decomposition of adsorbed organics and of the TEG coating. The total weight loss for the sample was 13%, with 3% of the total mass attributed to adsorbed water and the remaining 10% from the TEG coating of the nanoparticles. Thermograms for all samples showed similar shapes, and comparable percentages of total mass loss indicate all samples experienced similar mass loss processes.

Figure 3.6 shows the overlaid FT-IR spectra for each sample, zoomed into the v_1 absorbance region. The maximum of the v_1 peak can be seen to shift between approximately 510 and 536 cm^{-1}, with samples S20 and S22 being the most notably blue-shifted of the series. The movement of the v_1 maximum is indicative of Mn^{2+} movement into octahedral lattice sites, suggesting that longer dwell times may have some influence on cation distribution. However, this was not true for samples S16 or S17, indicating that dwell time is not the only controlling factor of cation distribution. Additionally, some samples synthesized with longer dwell times showed an increase in crystallite size, though this trend was not linear for all samples in the series.

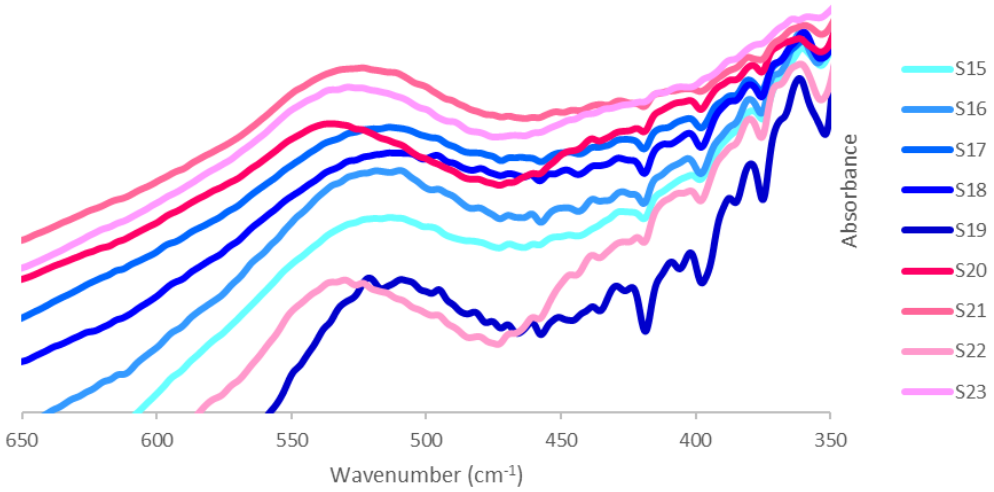

Figure 3.6. *Overlaid FT-IR spectra for all samples synthesized with a dwell.*

3.1.2 Concentration by solid and solvent volume

Changing the mass ratios of precursors can alter *x* from eq. 1.1. To create samples representative of a full concentration gradient, Fe precursor concentration was varied between 1 and 8 mmol while maintaining the original 1:2 precursor ratio defined in section 2.1.2, along with a variation of TEG volume between 20 and 100 mL. These modifications comprised a total of 14 samples in the final material model.

Figure 3.7 shows the XRD patterns for all samples in the 100 mL series, where Fe precursor concentration was varied between 8 and 2 mmol. A fourth sample was attempted in 100 mL solvent and 1 mmol Fe precursor; however, this concentration was too low to offer a product of appropriate crystallinity and thus was excluded from the model. All XRD patterns show the characteristic peak around 34 °2θ in line with the reference pattern, though intensity of this peak decreases with solid content, and noisiness of the patterns indicates formation of a potentially amorphous or mixed phase product.

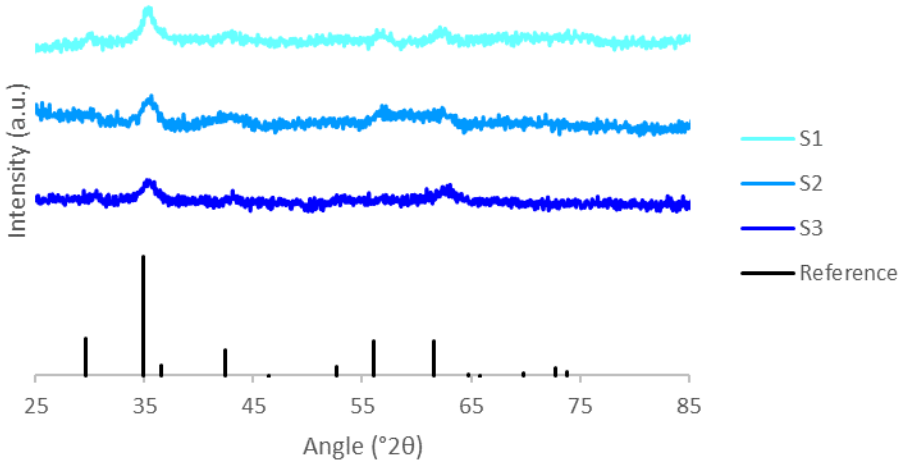

Figure 3.7. *XRD patterns for the samples synthesized in 100 mL solvent. Offset added for clarity.*

Crystallite size was minimized at 4.8 nm and 4 mmol Fe precursor (sample S2) and maximized at 7.3 nm and 8 mmol Fe precursor (sample S1). Sample S2 exhibited the greatest microstrain at 2.26%, indicating a greater number of defects in the crystal lattice and more stress than observed by either sample S1 or S3.

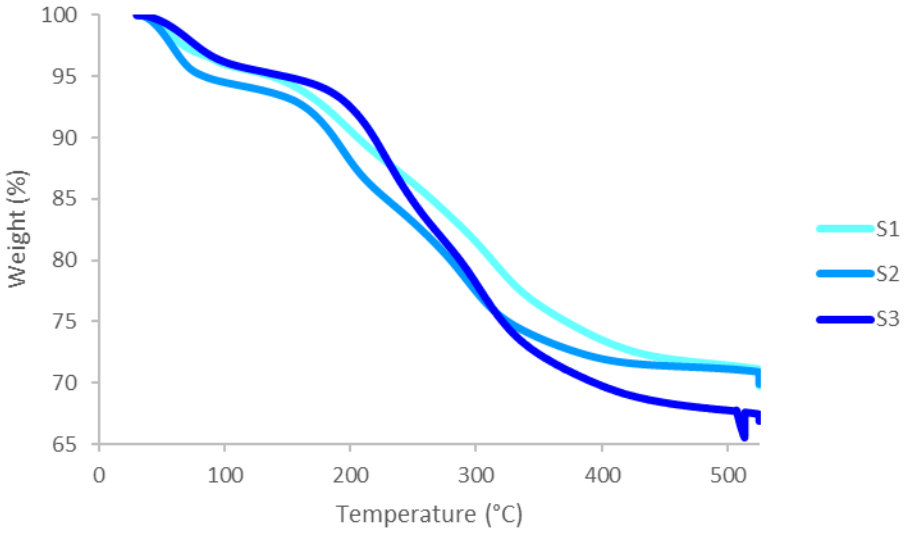

Figure 3.8. *Thermograms for all samples synthesized in 100 mL solvent.*

Figure 3.8 displays overlaid thermograms for all samples synthesized in 100 mL solvent. Fe precursor concentration was varied between 8 and 2 mmol, and all samples exhibited similar

quantities of TEG coating. Sample S3 showed a 5% increase in mass percentage of TEG coating; this is attributed to the low solid concentration relative to glycol volume. Sample S3 also exhibited an irregular data point around 500 °C, which is attributed to instrument error. All samples experienced similar decomposition steps, with the first step up to approximately 100 °C attributed to adsorbed water and the slow decomposition of the TEG beginning around 200 °C, where organics such as CO_2 are also presumed to exist on the particle surface.

A comparison of the v_1 peak location for all samples synthesized in 100 mL of solvent is shown in Figure 3.9. The peak maximum did not shift, indicating that these syntheses were not successful in producing any difference in cation distribution within the crystal lattice. Sample S1 showed the greatest definition in absorbance peak, which may be due to discrete differences in pellet composition. No differences in peak shape were observed, though the diffraction peak corresponding to the (220) crystal plane around 29 °2θ is hardly observed.

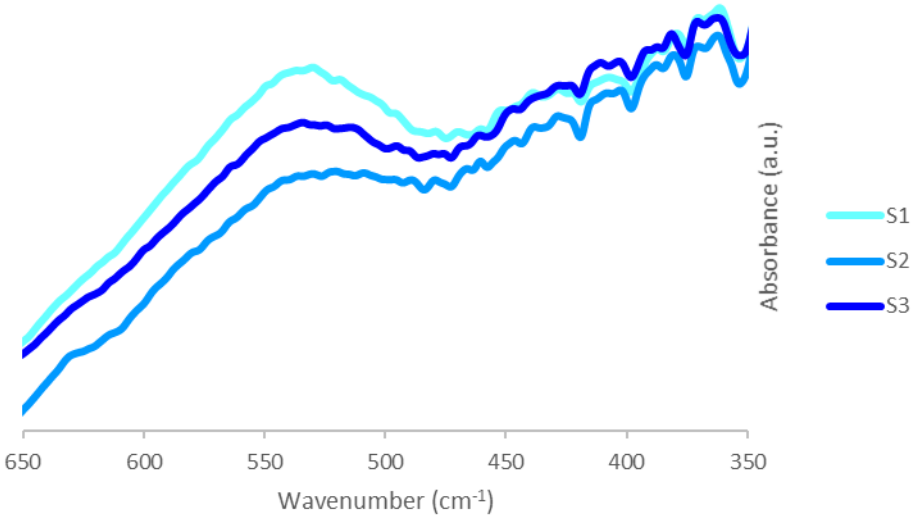

Figure 3.9. *Overlaid FT-IR spectra comparing the v_1 peak location for all samples synthesized in 100 mL solvent.*

Figure 3.10 provides the overlaid XRD patterns for all samples synthesized in 80 mL of solvent. Fe precursor concentration was varied between 8 and 1 mmol, where samples S6 and S7 show more amorphous profiles, characteristic of the lower concentration syntheses. As solid content increased, crystallinity appeared to improve, particularly for sample S4.

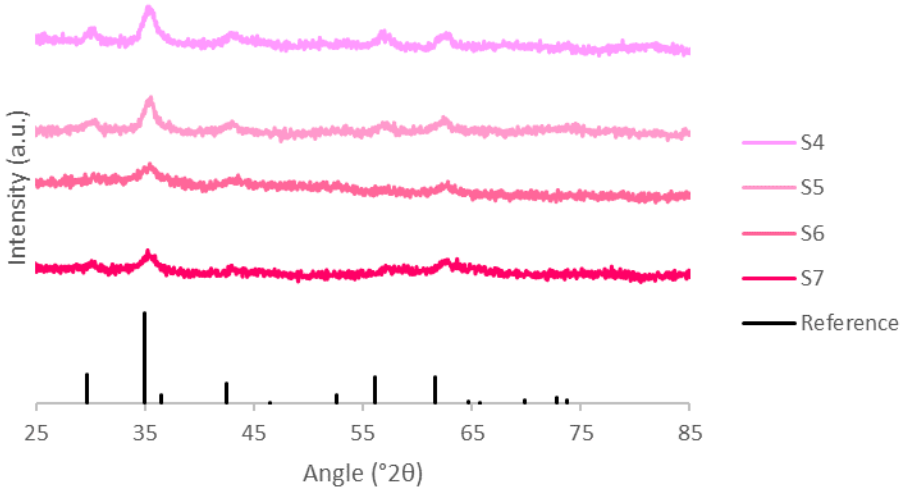

Figure 3.10. *XRD patterns for all samples synthesized in 80 mL solvent. Offset added for clarity.*

Crystallite size for the samples in Figure 3.10 were 7.12 ± 1.13 nm, with a minimum lattice parameter of 8.31 Å and maximized microstrain for sample S7 at 2.06%. These values, along with the decrease in intensity of the diffraction peak around 35 °2θ, support a more amorphous or mixed phase composition for sample S7 relative to others in the series. The peak corresponding to the (220) crystal plane can be seen gaining intensity as Fe precursor concentration increases, being the most defined for sample S4.

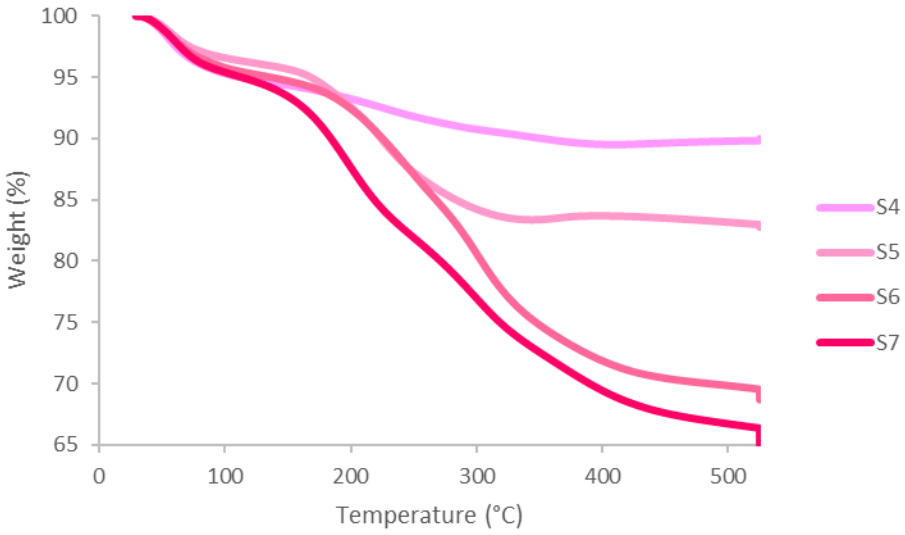

Figure 3.11. *Overlaid thermograms for samples synthesized in 80 mL solvent.*

Thermograms for all samples synthesized in 80 mL of solvent are displayed in Figure 3.11. Samples S6 and S7, synthesized at the lowest solid precursor concentrations, showed similar

quantities of TEG coating to the samples in the 100 mL series in Figure 3.8 (27 and 31%, respectively).

TEG coating was minimized at 5% for sample S4 and maximized at 31% for sample S7. A reduction in TEG coating was observed for samples S4 and S5, along with an improvement in XRD intensity in Figure 3.10. Sample S5 showed a slight increase in mass beginning around 350 °C; this could potentially be due to instrumental error.

Figure 3.12 displays the overlaid FT-IR spectra, focused on the v_1 region, for the samples synthesized in 80 mL of solvent. Peak maxima were very similar, occurring within ±1.30 of 530.58 cm^{-1}. Peak shape also did not appreciably change, exhibiting lack of movement of cations within the crystal lattice.

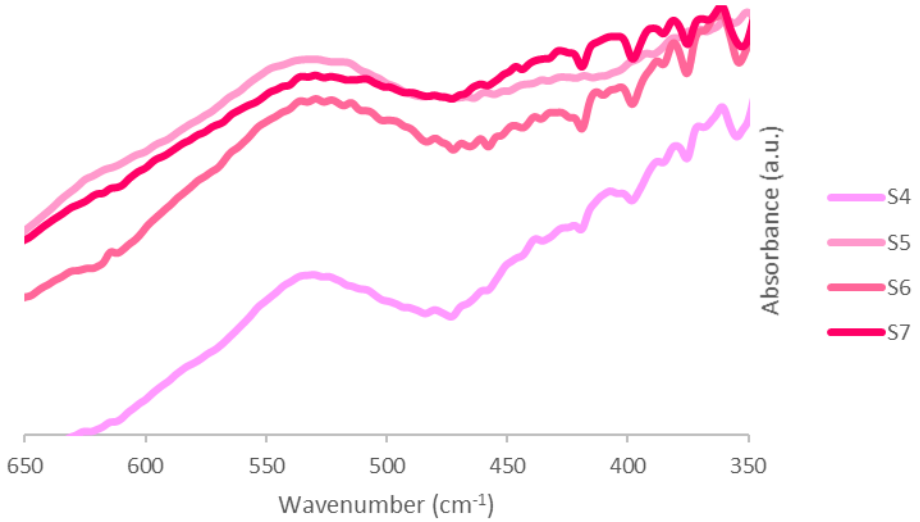

Figure 3.12. *Overlaid FT-IR spectra for all samples synthesized in 80 mL solvent.*

Figure 3.13 displays XRD patterns for all samples synthesized in 50 mL solvent, with Fe precursor concentration varied between 8 and 1 mmol. All concentrations produced similar diffraction patterns, with a relatively well-defined characteristic peak around 35 °2θ. A slight spike before the characteristic peak in sample S10 is observed and is attributed to instrument noise.

Average crystallite size was 7.05 ± 0.89 nm for the series. Lattice parameter was minimally impacted by synthetic condition at 8.41 ± 0.01 Å, and microstrain was 1.46 ± 0.11%. Peak intensities are relatively equal, evidence that differences in solid content had little influence on crystallinity.

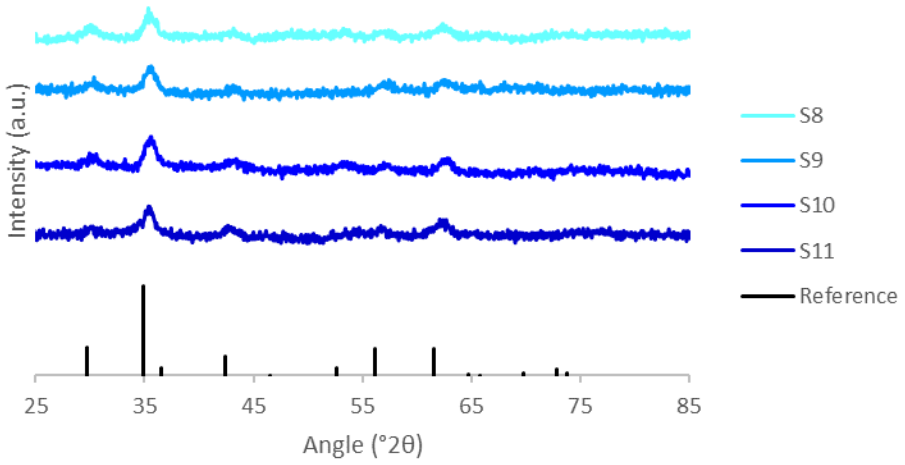

Figure 3.13. *XRD patterns for all samples synthesized in 50 mL solvent. Offset added for clarity.*

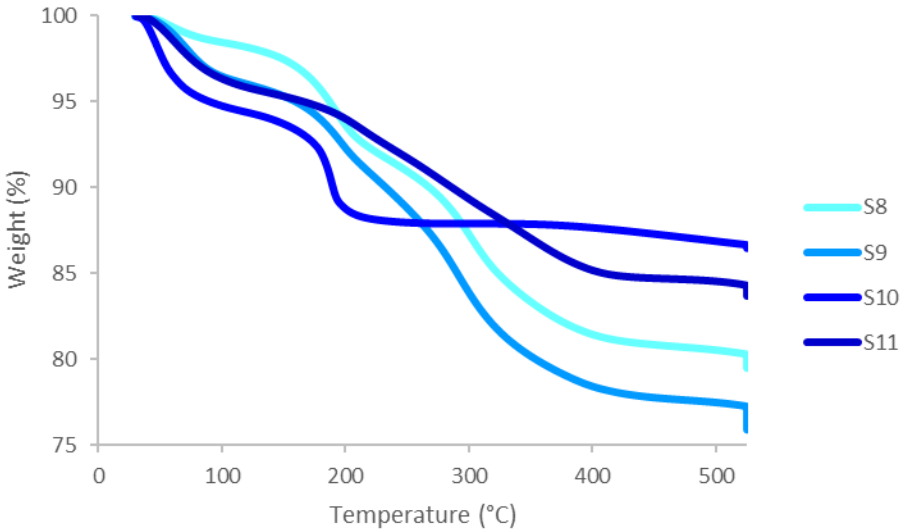

Figure 3.14. *Thermograms for all samples synthesized in 50 mL solvent.*

Figure 3.14 displays overlaid thermograms for all samples synthesized in 50 mL of solvent. Samples all followed the same general weight loss pattern with sample S10 serving as a notable exception. Sample S10 shows a 5% loss up to 100 °C, with another sharp 5% drop around 200 °C, followed by a plateau. This plateau after 200 °C is irregular, and indicates the nanoparticles were not sufficiently coated with TEG.

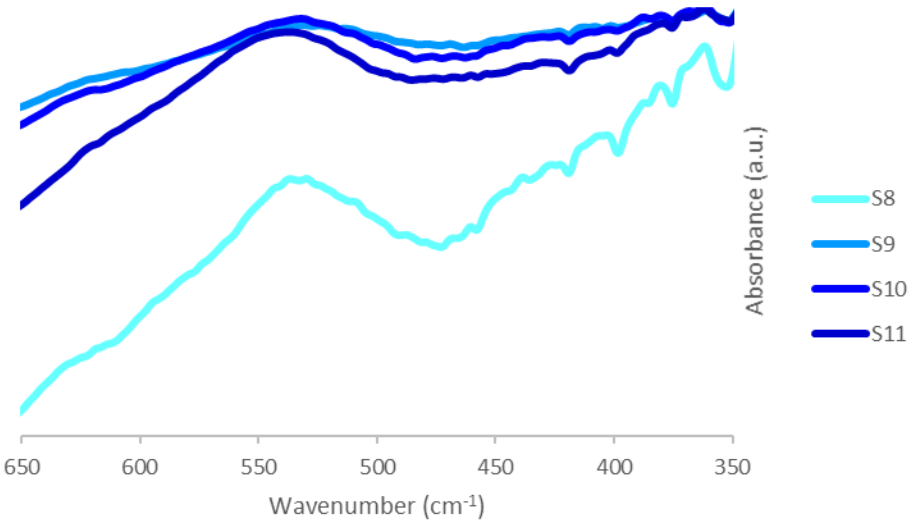

Figure 3.15. *Overlaid FT-IR spectra for all samples synthesized in 50 mL solvent.*

Figure 3.15 displays the overlaid FT-IR spectra for all samples synthesized in 50 mL of solvent. The v_1 maximum was slightly offset for sample S11, located at 537.09 cm^{-1}, while samples S8, S9, and S10 fell within ±1 of 530.98 cm^{-1}. From eq. 2.6, this indicates movement of 3.27% of Mn^{2+} into octahedral lattice sites for sample S11.

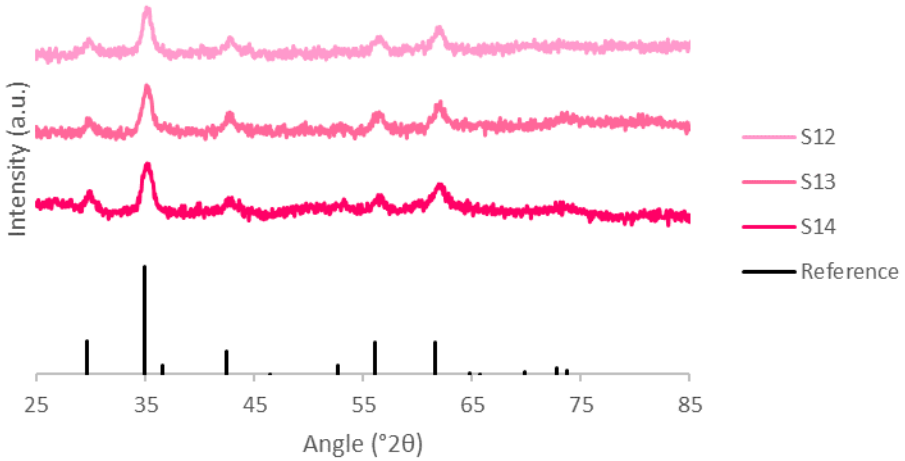

Figure 3.16. *Overlaid XRD patterns for all samples synthesized in 20 mL solvent. Offset added for clarity.*

Figure 3.16 shows overlaid XRD patterns for all samples synthesized in 20 mL solvent. Fe precursor was varied between 4 and 1 mmol. At 8 mmol, the reaction flask was too concentrated to produce a crystalline product, and that condition was excluded from the model.

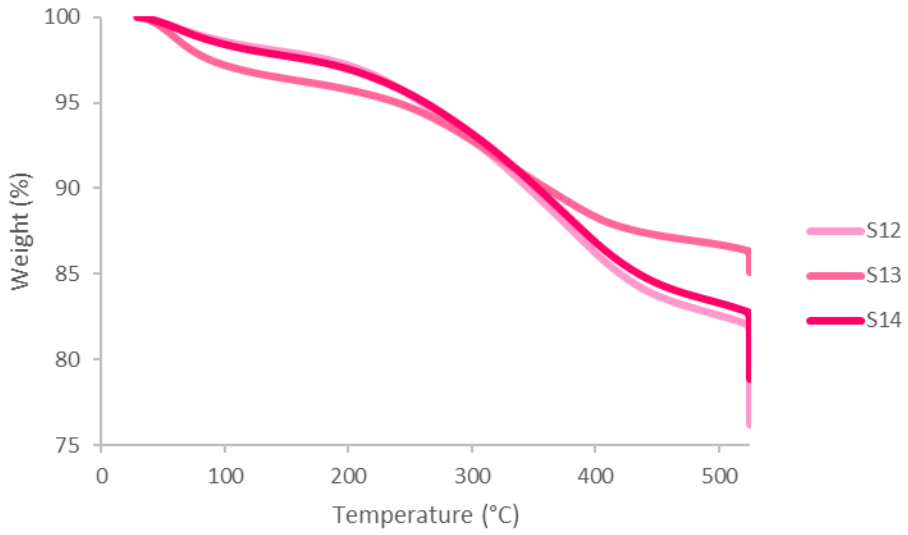

Figure 3.17. *Thermograms for all samples synthesized in 20 mL solvent.*

The XRD patterns in Figure 3.16 show the greatest definition of all within this chapter, owing to the low solvent volume. Characteristic peaks for the (220), (311), (511), and (440) planes are all visible. Average crystallite size for the 20 mL series was 11.07 ± 1.08 nm, with lattice parameter varying less than 0.01 Å among all samples. The lowest microstrain occurred in sample S14 at 1.13%.

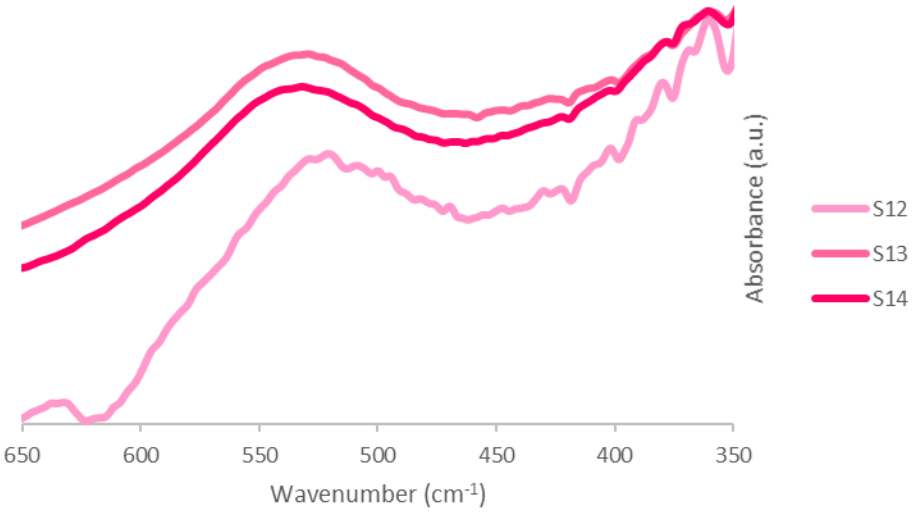

Figure 3.18. *FT-IR spectra for all samples synthesized in 20 mL solvent.*

Thermograms for all samples synthesized in 20 mL of solvent are overlaid in Figure 3.17. All samples showed similar weight loss patterns, but masses varied between 10 and 21%. The mass

of TEG coating was not concentration dependent; it was maximized for sample S13, which was synthesized at the greatest solid concentration, 4 mmol.

FT-IR spectra for all samples synthesized in 20 mL of solvent are shown in Figure 3.18. While the shape of the v_1 peak did not change, the peak location shifted from 520.69 cm^{-1} for sample S12 to 532.27 cm^{-1} for sample S14. This v_1 shift indicates some change in bonding within the crystal lattice.

3.1.3 Stir rate

A modification of synthetic transport properties was attempted by varying the synthetic stir rate at either 500 or 900 rpm, as shown in Table 3.2. Stir rates below 500 rpm were deemed too slow at low concentrations to form appropriate crystals for analysis, while speeds above 900 rpm were not appropriate for synthesis at low volumes.

All parameters determined by XRD, TGA, and FT-IR are detailed in Table 3.3. No linear trends were observed between any of the obvious synthetic modifications, indicating that the modifications used here were not alone suitable to understand their impact on material properties (size or cation occupancy). To better understand their relationship to the synthetic variations, these values served as supplementary variables for the modeling detailed in Chapter 4.

Table 3.3. *Quantifications from Preliminary Characterization Methods*

Sample ID	Size (nm)	Lattice (Å)	Microstrain (%)	Shell Mass (%)	ν_1 (cm^{-1})
S1	7.3	8.43	1.60	25	529.85
S2	4.8	8.46	2.26	25	520.69
S3	5.4	8.31	1.98	30	534.19
S4	8.0	8.41	1.44	5	530.34
S5	7.5	8.43	1.53	13	532.75
S6	7.8	8.45	1.45	27	529.37
S7	5.2	8.31	2.06	31	529.85
S8	7.9	8.40	1.37	16	529.85
S9	7.3	8.40	1.51	19	531.30
S10	5.8	8.42	1.37	9	531.78
S11	7.2	8.41	1.60	15	537.09
S12	12.3	8.48	1.22	21	520.69
S13	10.3	8.47	1.21	10	529.85
S14	10.6	8.48	1.13	14	532.27
S15	8.1	8.48	1.45	11	513.46
S16	8.6	8.47	1.42	13	510.09
S17	11.4	8.46	1.09	9	513.94
S18	8.9	8.47	1.33	15	513.94
S19	8.3	8.46	1.42	10	521.18
S20	11.7	8.45	1.07	9	536.12
S21	11.5	8.45	1.04	10	523.59
S22	7.5	8.41	1.49	12	530.34
S23	9.1	8.42	1.28	10	528.89

3.1.4 Size Validation

Crystallite size was calculated for all samples using eq. 2.2 on the FWHM of the peak around 29 °2θ. Average crystallite size tends to be smaller than the whole particle, and TEM was performed on a subset of samples to validate the particle sizes against calculations from eq. 2.2. These images further validate the synthetic methodology for MH applications, where the uniform size and shape distribution is reproducible between syntheses.

Figure 3.18 shows three images for sample S19. The particles can be seen to be uniformly spherical, with no obvious size discrepancies. A histogram of particle size distribution is offered

in Figure 3.19, where particle size was found to be 8.93 ± 1.21 nm. These sizes are slightly larger than the XRD calculated size of 8.3 nm.

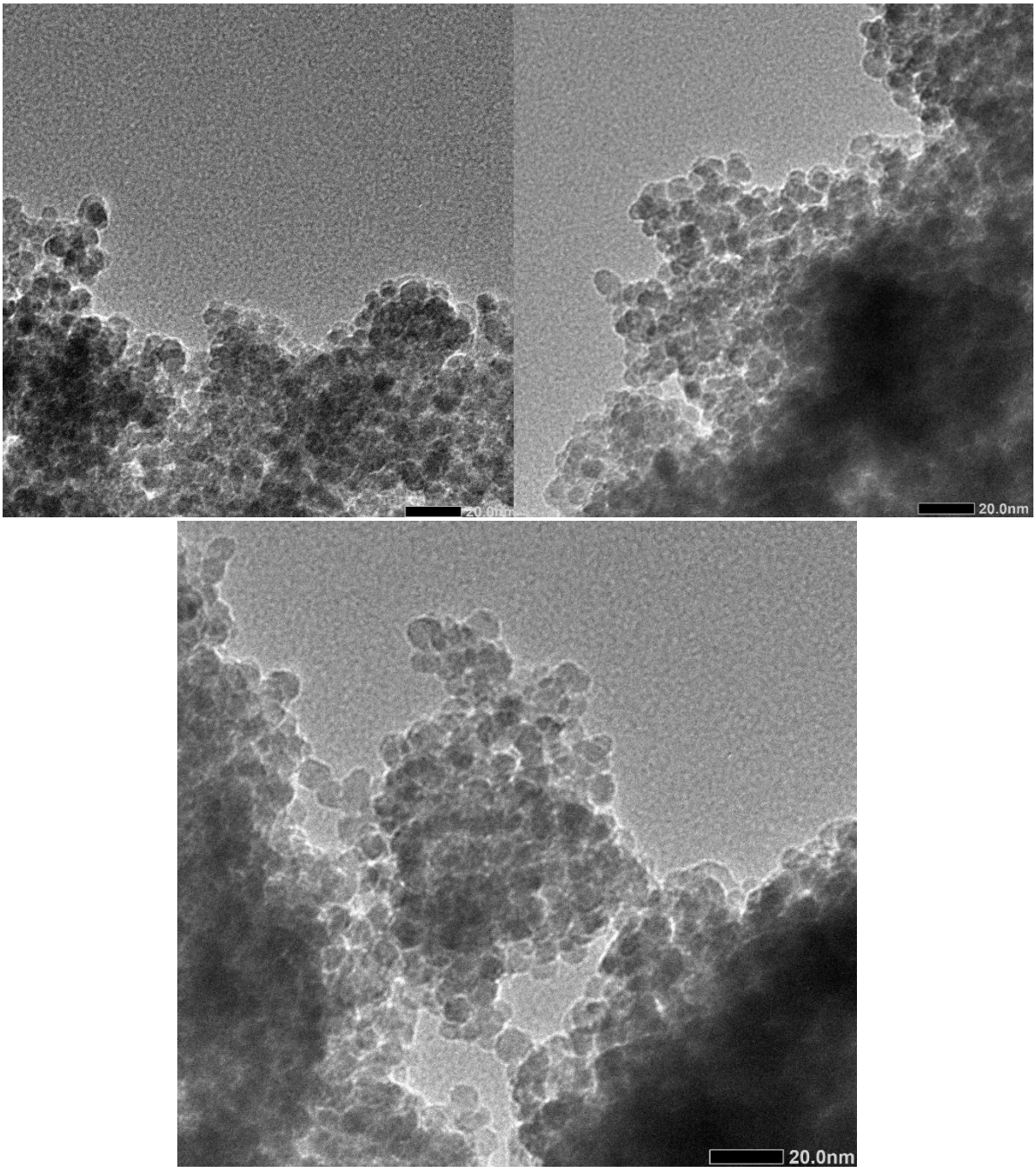

Figure 3.18. *TEM images for sample S19.*

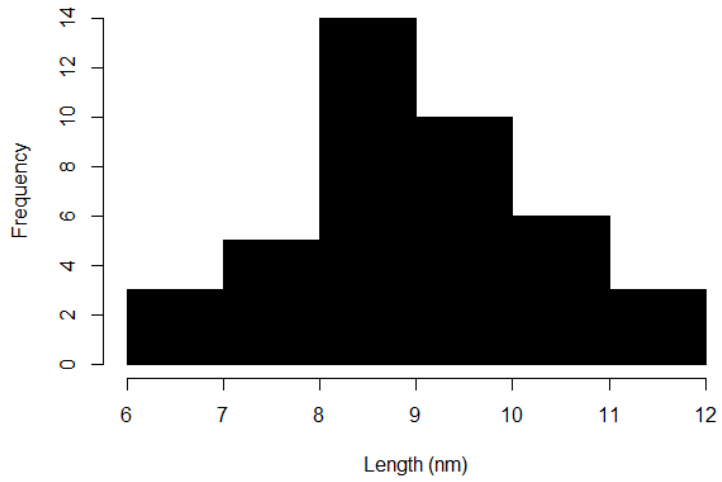

Figure 3.19. *Histogram of particle diameters for Sample S19.*

Figure 3.21 displays selected TEM images for sample S20. TEM again confirmed a uniform size distribution of spherical particles, with some clustering potentially due to self-attraction of the particles. The average particle size for sample S20 was 8.76 ± 1.29 nm, which is smaller than the XRD calculations of 11.7 nm (Figure 3.20). This could be due either to peak broadening of the XRD pattern skewing calculations, or self-attractions of the nanoparticles offsetting the diffraction pattern.

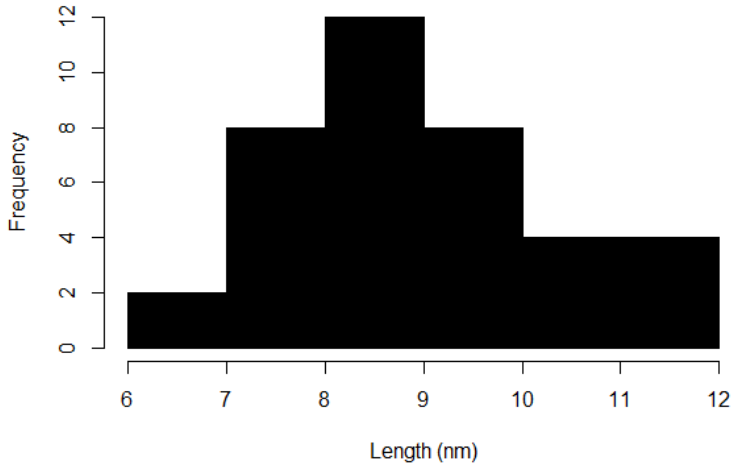

Figure 3.20. *Histogram of particle diameters for sample S20.*

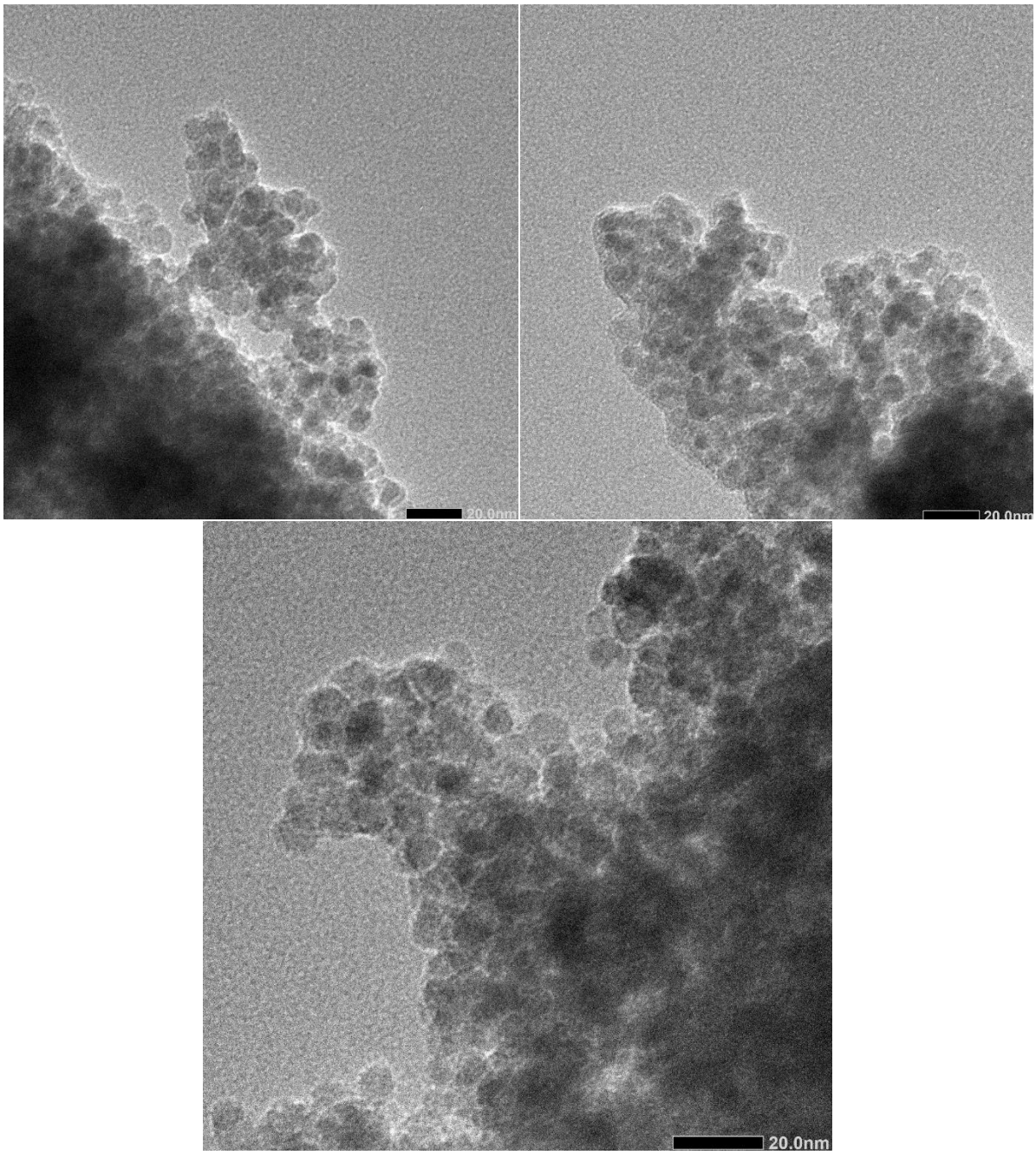

Figure 3.21. *TEM images for sample S20.*

Chapter 4. Statistical Modeling and Chemometrics

4.1 Modeling

Statistical modeling was utilized to explore the multifactor opportunity space presented by the test set outlined in Table 3.2. From the results given in Table 3.3, no obvious trends could be identified among the synthetic conditions. However, the changes in material properties, specifically size and v_1 peak location, indicate that synthetic modifications were impacting the material structure.

4.1.1 Principal Component Analysis

Principal component analysis (PCA) is an unsupervised, multivariate technique used for exploratory analysis and predictive modeling in complex datasets. By reducing the dimensionality of the sample space, the visualization of complex information and the identification of patterns becomes possible, enabling clarification of underlying dissimilarities.[96] This dimensionality reduction results in a small number of independent linear combinations that capture as much of the original variability of the dataset as possible.[97]

PCA creates a matrix $\boldsymbol{X}=\{x_{ij}\}$ of size $I\times J$, where I is the number of samples and J is the number of variables, that is decomposed into

$$X = T_A P^t{}_A + E \tag{4.1}$$

where A is the number of principal components, $T_A=\{t_{ia}\}(I\times J)$ is the scores matrix, $P_A=\{p_{ja}\}(J\times A)$ is the loadings matrix, and $E=\{e_{ij}\}$ is the residuals matrix.[98] The principal components belong to a variable space composed of unit vectors, where the i-th vector is a line that best fits the data and is orthogonal to the first i-1 vectors (PC 1 labeled in Figure 4.1).[99] This line of best fit minimizes the average squared distance from all datapoints back to that line. PCA involves computing these principal components in order to perform a change of basis on the data. The principal components are the eigenvectors of the covariance matrix, and the proportion of variance that each eigenvector represents is calculated by dividing the corresponding eigenvalue by the sum of all eigenvalues. Once most of the information is captured, the remaining components can be reasonably ignored.[99]

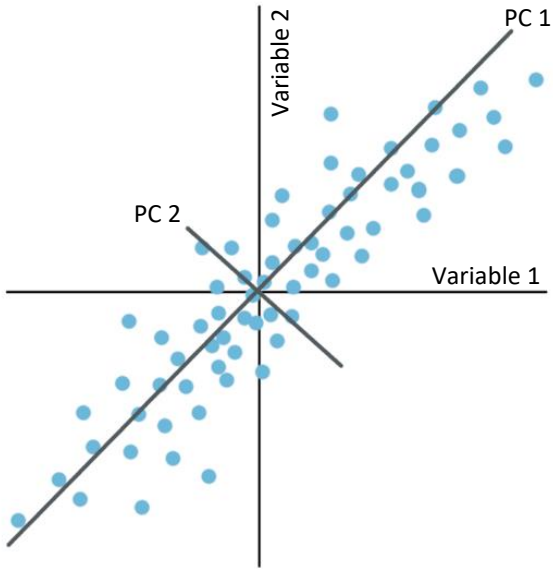

Figure 4.1. *Two-dimensional representation of a PCA score plot. Adapted from Beebe et. al.*[99]

For any PCA, a score is assigned to each observation in the dataset, and a score plot measures the distance for each of these from the origin along the loading vector of the first component until the observation is projected onto the direction vector. The first score vector belongs to the greatest source of variation in the dataset, and the following scores are attributed to the next greatest sources of variation, in descending order.

PCA was utilized as an exploratory analysis to uncover hidden variance on the 23 samples outlined in Table 3.2. For this work, the PCA was performed on the correlation matrix. Correlations were selected over covariances or unscaled data due to the variety in data (many different units and measurements).[100] In the analysis, each variable was standardized to unit norm.[97]

The analysis was conducted using JMP Pro 15.1 statistical software. Independent variables in the test set were those in Table 3.2: molar concentration of iron precursor, solvent volume, spin speed, and dwell time. Supplementary variables included those in Table 3.3: crystallite size, lattice parameter, quantity of glycol shell coating, microstrain, and maximum absorbance of the v_1 region. Supplementary variables do not influence the PCA, and simply serve to assist in interpreting the dimensions of variability.

Variance is systematic in a multivariate dataset, and multiple components are often necessary to fully describe the dataset. The second principal component is orthogonal to the first, and together they define a plane of the *K*-dimensional variable space. These coordinates are the scores that make up the score plot, which explores relationships between variables to reveal

groups or trends.[98] Covariances are used to interpret correlations. If positive, the two variables are correlated. If negative, the two variables have an inverse correlation.

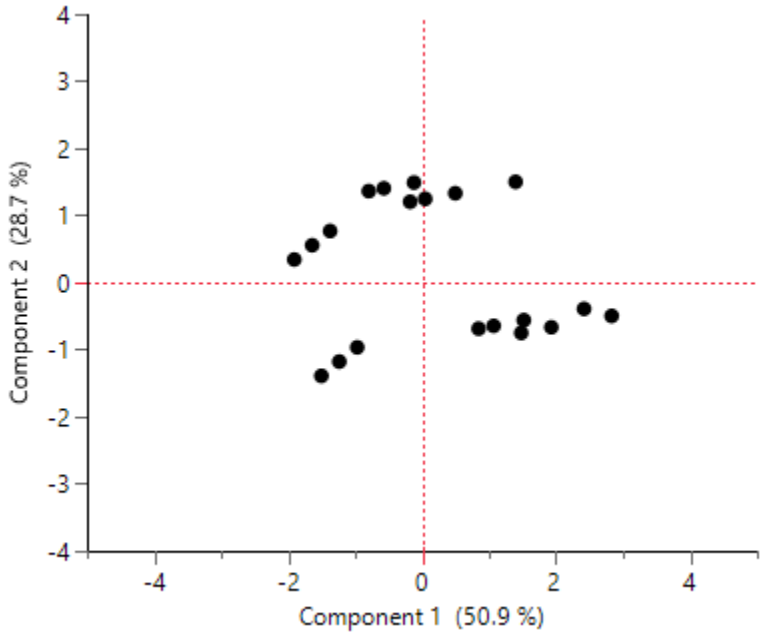

Figure 4.2. *Score plot for the first two principal components.*

Figure 4.2 displays the score plot for the first two principal components, where the black dots represent individual scores. The first component can be seen on the *x*-axis, and the second component on the *y*-axis. Several clusters can be noticed though little other information is offered by the plot beyond the observation that 50.9% of the variance is associated with the first principal component and 28.7% is associated with the second.

A loading matrix, or biplot, depicts the influence of each characteristic on a principal component and tends to be the most informative part of a PCA.[96,98] Small angles are indicative of positive correlations, while large angles are indicative of negative ones. A 90° angle shows no correlation between two variables.

The biplot for the first two principal components is shown in Figure 4.3. Independent variables are represented by red arrows, and supplementary variables are represented by the blue arrows. Axes are defined the same as in Figure 4.2. Data labels are as follows, in accordance with Table 3.2: “TEG” is TEG volume, “[FeAcAc]” is Fe precursor concentration, “Dwell” is dwell time, and “Speed” is stir rate. For supplementary variables, “Microstrain”, “Size”, and “Lattice” all correlate as defined with what is given in Table 3.3. “Shell” references the mass percentage of TEG coating, and “Max abs” is the v_1 peak location.

Two variables are seen to have a positive correlation with component 1: TEG volume and Fe precursor concentration. Dwell is negatively associated with both components, and stir rate is only positively correlated with component 2. From Figure 4.3, it can be seen that TEG volume is the only independent variable positively correlated with component 1 alone, and thus is attributed to the 50.9% variance observed. Shell and microstrain are also positively correlated with component 1, indicating association.

The second principal component is attributed to stir rate. Crystallite size and lattice parameter are very lightly correlated with component 2, indicating moderate influence of stir rate. Fe precursor concentration showed a positive correlation with both components, indicating indirect influence on sample properties. This is potentially correlated with the v_1 peak location. Dwell time showed no influence on either component, and did not correlate with any supplementary variables.

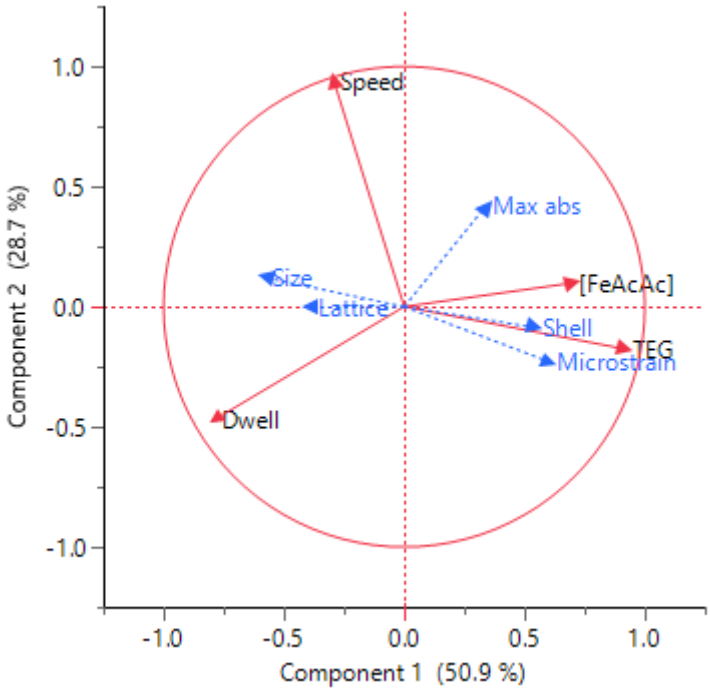

Figure 4.3. *The loading matrix for the first two components, which provides a breakdown of principal components by variable.*

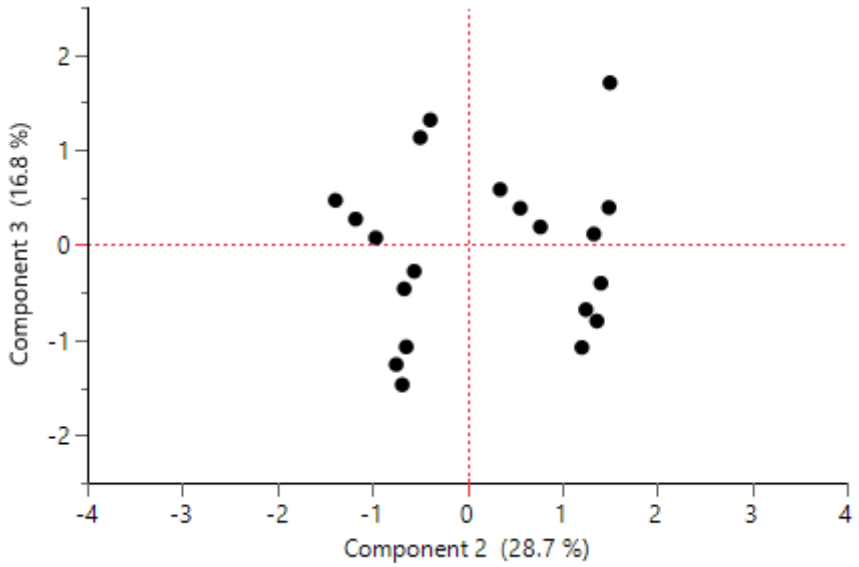

Figure 4.4. *Score plot offering the PCA breakdown of component 2 versus component 3.*

The score plot for the second and third principal components is given in Figure 4.4. As seen in Figure 4.3, 28.7% of the total sample variance is associated with component 2. The third principal component accounts for another 16.8% of the total sample variation.

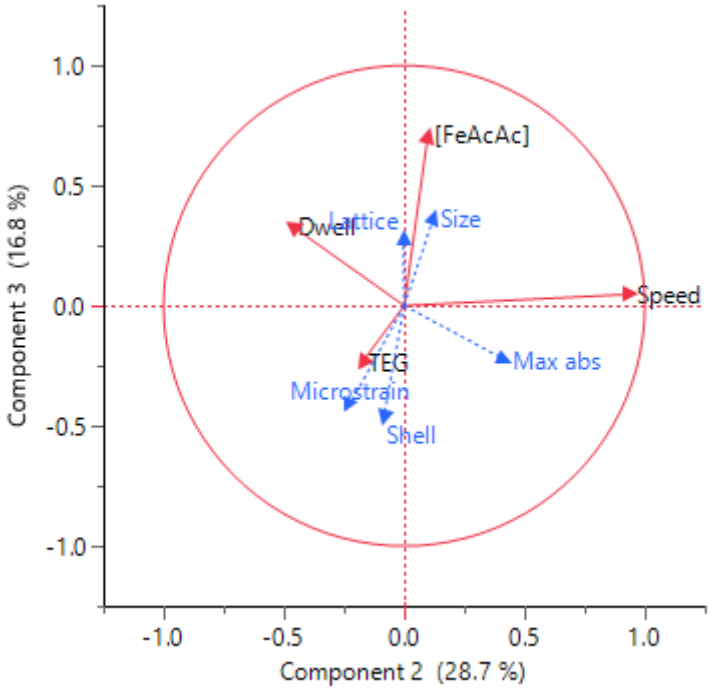

Figure 4.5. *PCA breakdown by variable for components 2 and 3.*

The biplot for Figure 4.4 is shown in Figure 4.5, where stir rate and Fe precursor concentration are positively correlated with both component 2 and 3. TEG volume was negatively correlated with both components, indicating no influence on either. Dwell time was positively correlated with component 3, indicating influence with the lattice parameter. The association of stir rate and Fe precursor concentration with both components 2 and 3, while in Figure 4.3 stir rate was only positively correlated with component 1, is attributed to residual effects.

A Scree plot provides a visual comparison of eigenvalue sizes by showing how much variation is captured by each component. Because the majority of influence is usually explained by the first few components, a scree plot helps to visualize which components should be retained, and which can be reasonably ignored. An acceptable scree plot has several distinct features: a steep drop, an elbow-shaped bend, and a flatline. The elbow defines the cut-off point for important and unimportant information. If a scree plot does not match the ideal visuals, the Kaiser rule can be added to the analysis, where only eigenvalues larger than 1 are selected as important. Additionally, it would be ideal for the selected components to describe at least 80% of the total sample variance. Too many components are indicative of poor fit of PCA to the dataset.[100]

Table 4.1. *Eigenvalues for Each Principal Component*

Component	Eigenvalue
1	2.0354
2	1.1462
3	0.6729
4	0.1454

Eigenvalues for each component are given in Table 4.1. In Figure 4.6, the number of components is shown on the *x*-axis and the eigenvalue is shown on the y-axis. Each black dot depicts one component, and the red connecting line provides a guideline to visualize the variance between each component. A slight shoulder can be seen around component 3, but this visual is not sufficient, as the plot fails to level out.

For this dataset, the Kaiser rule was used to determine which components to retain; components 1 and 2 both had eigenvalues larger than 1, and were accepted as the most influential variables. These two components accounted for 79.6% of the total sample variance, indicating reasonable fit of the data to PCA. Component 3 produced an eigenvalue of 0.6729, and was retained. Component 4 was the least significant and was ignored.

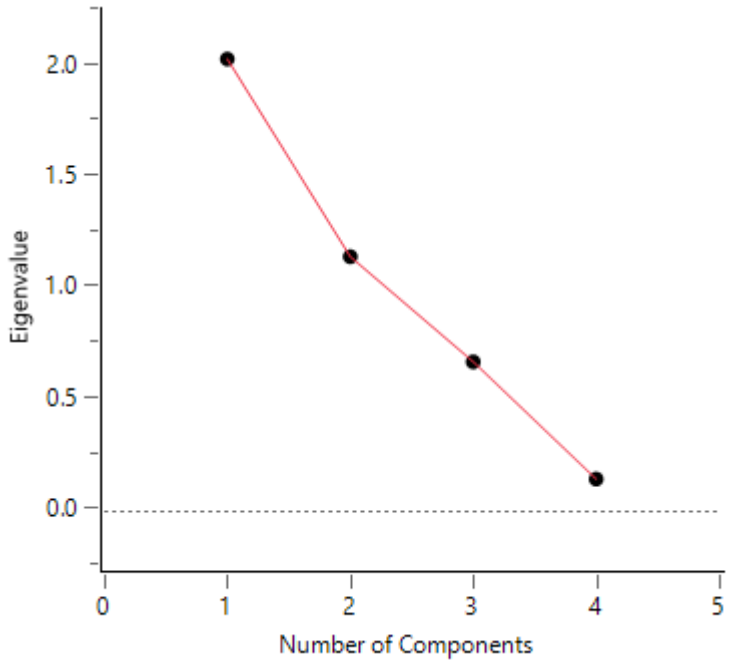

Figure 4.6 *Scree plot for the four components in the analysis.*

The outlier analysis provides T^2 values for all variables in the analysis. T^2 is calculated as

$$T_i^2 = X_{ci} P_A L^{-1} P_A^T X_{ci}^T \tag{4.2}$$

where P_A is a matrix containing the first A eigenvectors, L is a diagonal matrix containing the first A eigenvalues, and X_{ci} is the standardized data for the i^{th} observation. Both the median and the UCL are calculated as

$$CL_{T^2,q} = \frac{(n-1)^2}{n} \beta\left[q, \frac{A}{2}, \frac{n-A-1}{2}\right] \tag{4.3}$$

where n is the number of observations and $\beta\left[q, \frac{A}{2}, \frac{n-A-1}{2}\right]$ is the q^{th} quantile of the β $\left(\frac{A}{2}, \frac{n-A-1}{2}\right)$ distribution. For median calculations, q=0.5, and for UCL, q=(1-α).[100]

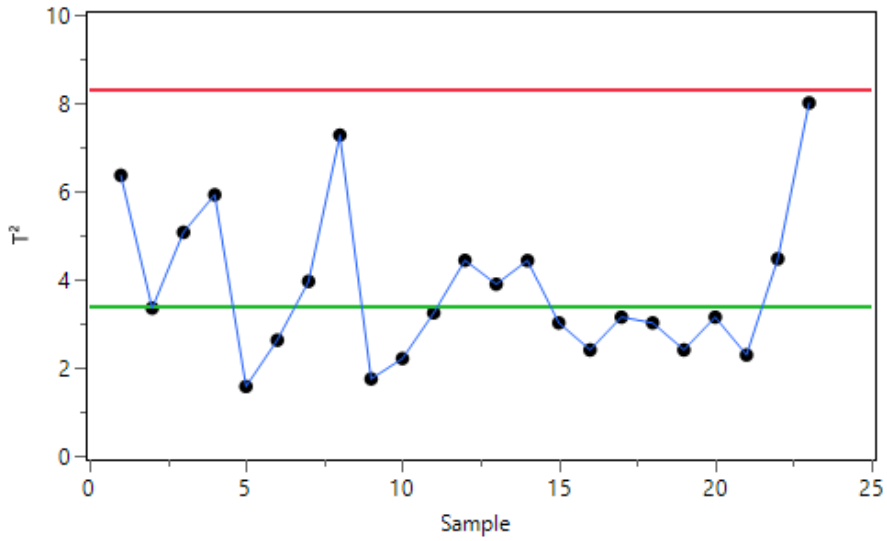

Figure 4.7. *Outlier analysis for all variables in the PCA. The green line represents the median, the red line the upper control limit, and the blue lines depict the distance between each variable.*

Figure 4.7 displays the T^2 contribution plots for all 23 samples in the model. Each plot displays the independent variables of the PCA on the *x*-axis and the contribution proportion on the *y*-axis. The contribution of each variable to the respective sample variance is represented as a bar. Samples showed a range of variance, with each variable producing a range of contribution to each sample. Horizontal lines are shown at the median (green, 3.41) and the upper control limit (UCL) (red, 8.29). An α value of 0.05 was used to compute the upper control limit. No outliers were observed for the test set.

Figure 4.8 provides the T^2 contribution proportion plots for all samples in the test set. Samples are numbered according to the naming conventions defined in Table 3.2. Independent variables are shown on the *x*-axis, and contribution proportion is on the *y*-axis. The proportion of contribution is represented as a bar. Each sample experienced a range of contribution from each variable, where only one sample was influenced by a single variable, and another 17% were only influenced by two variables. Figure 4.8 aids in the visualization of the multivariate nature of the test set, where multiple synthetic conditions can be attributed to variance for a single sample. Additionally, it was noteworthy that no identifiable pattern exists between samples.

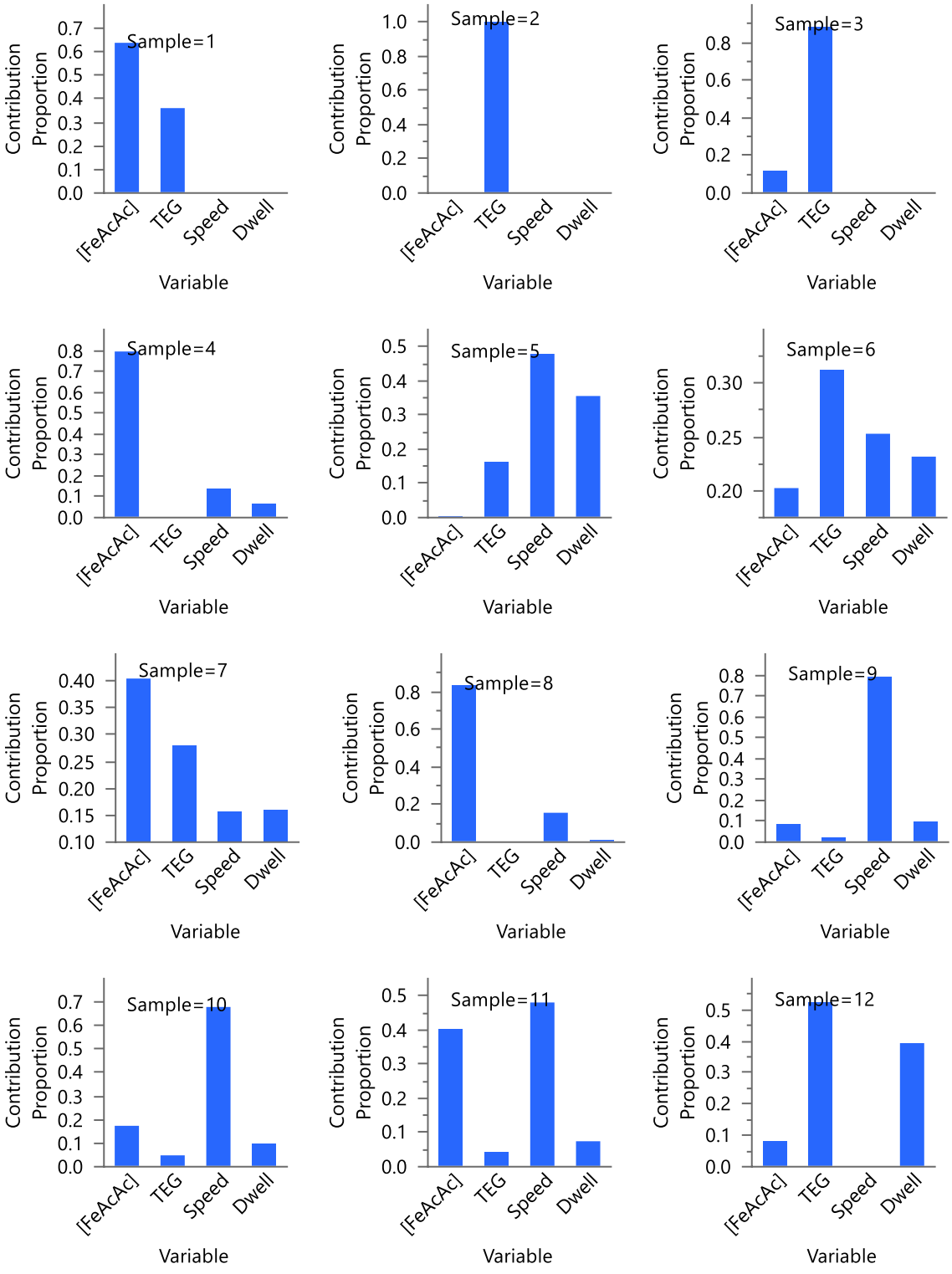
Sample=1
Sample=2
Sample=3
Sample=4
Sample=5
Sample=6
Sample=7
Sample=8
Sample=9
Sample=10
Sample=11
Sample=12
Contribution Proportion
Variable
[FeAcAc]
TEG
Speed
Dwell

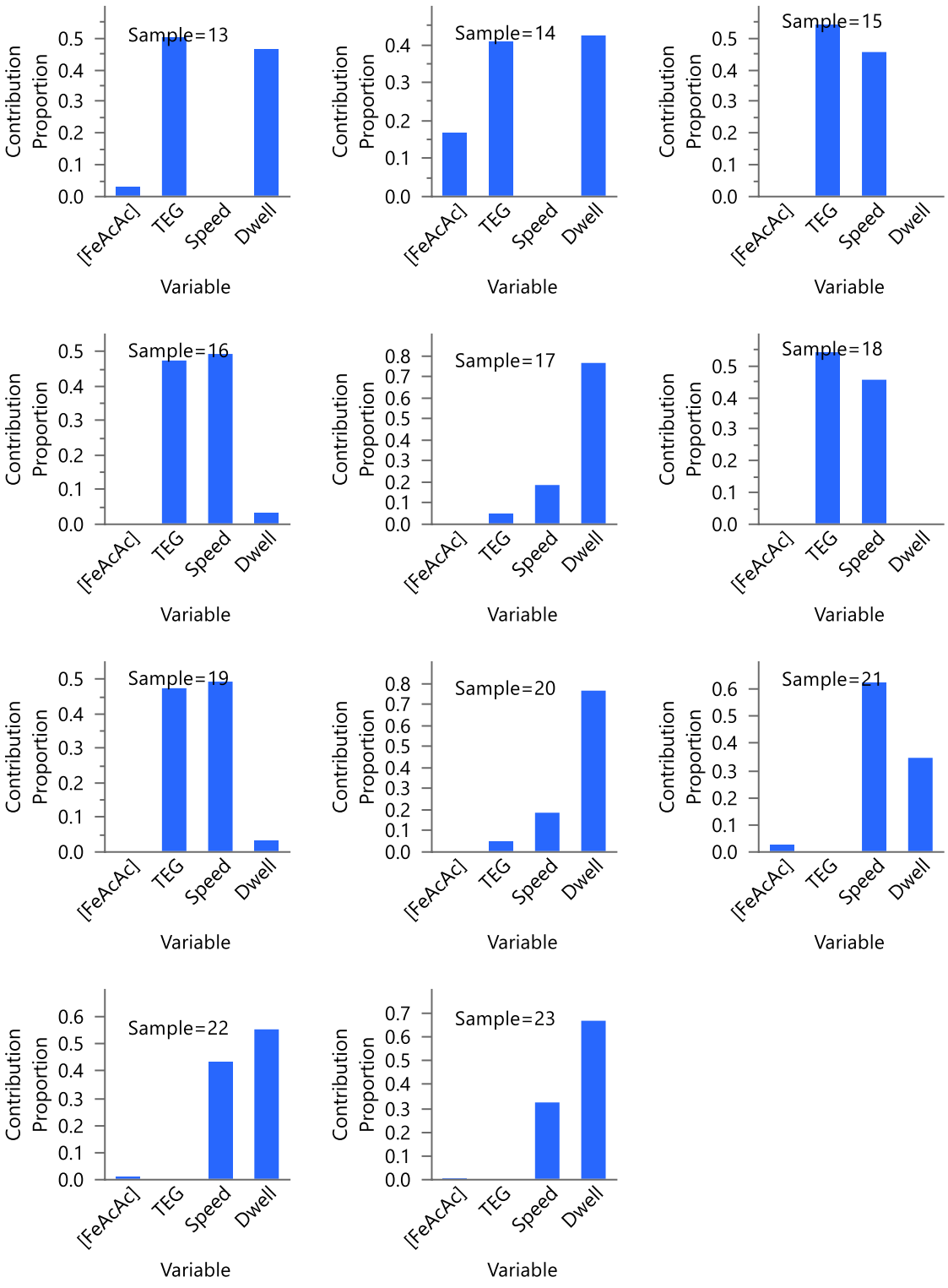

Figure 4.8. *T^2 contribution proportion plots for all samples in the PCA.*

4.2 Statistical Inferences

The impact of the first component, TEG volume, was presumed to be the result of concentration differences during synthesis, with low concentrations leading to more amorphous product and high concentrations leading to more crystalline product. Additionally, larger particle sizes were achieved at lower TEG concentrations. Stir rate, the second principal component, was influential in the hydroxide to oxide conversion, confirmed by TGA and IR measurements. The third and final principal component, dwell time, is attributed to a reduction in the polydispersity of the nanoparticles. Increasing dwell times tends to improve crystallinity, where particles may have experienced longer periods of molecular reorganization.

Supplementary variables of interest were crystallite size, which showed little correlation with any principal component. Additionally, v_1 peak location did not appear to be correlated with any synthetic condition. TGA volume showed strong correlation with both the quantity of coating on the particles and with microstrain. The PCA results were used to inform a subset of samples for magnetic characterization, which is described in chapter 5.

Chapter 5. Identifying an Optimal Synthetic Method to Maximize Saturation Magnetization

5.1 Constructing a Material Model

PCA results were used to inform the selection of a subset of samples for magnetics measurements that encompassed the full spread of variance, both in independent and supplementary variables. The model encompassed a range of both significant independent variables (TEG volume, stir rate, and dwell time), along with a full range of size and v_1 peak location. The synthetic conditions for these samples are outlined in Table 5.1.

Table 5.1. *Selected Sample Subset for Magnetics Measurements*

Sample ID	Fe precursor concentration (mmol)	TEG volume (mL)	Stir rate (rpm)	Dwell time (min)
S5	4	80	500	0
S11	1	50	900	0
S12	4	20	900	0
S16	2	20	500	120
S19	2	20	500	120
S20	2	20	500	150
S21	2	20	900	90

Sample stoichiometry was minimally affected by synthetic modifications, though samples synthesized at the lowest concentrations showed slightly more amorphous XRD profiles than those at high concentrations. No impurities were observed in any diffraction patterns, Figure 5.1. The average crystallite size varied between 7.2 and 12.3 nm.

Thermograms for all samples in the subset are overlaid in Figure 5.2. The quantity of glycol coating the particles ranged from 9-25%. This encompassed the full range of values for TEG coating from the test set (Table 4.1). All samples experienced similar weight loss patterns, save for sample S5, which exhibited a slight weight gain beginning around 400 °C.

Overlaid FT-IR spectra for the test set are shown in Figure 5.3 between 350 and 750 cm^{-1}. The selected samples encompassed a v_1 peak shift between 510 and 537 cm^{-1}. This indicated octahedral occupancy of Mn^{2+} ranged between -16 and 3% (Table 5.2). There is some evidence that Mn^{2+} may prefer tetrahedral sites.[102] This is supported by IR measurements, as v_1 peak locations indicated most samples adopted a normal lattice structure, with only a few samples displaying positive percentages of octahedral site occupancies for Mn^{2+}.

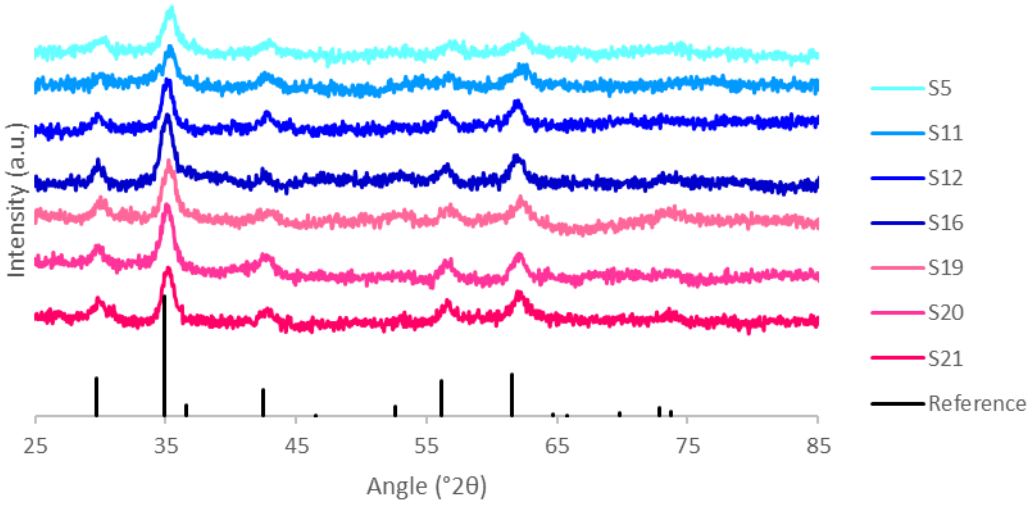

Figure 5.1. *Overlaid XRD patterns for all samples in the selected subset.*

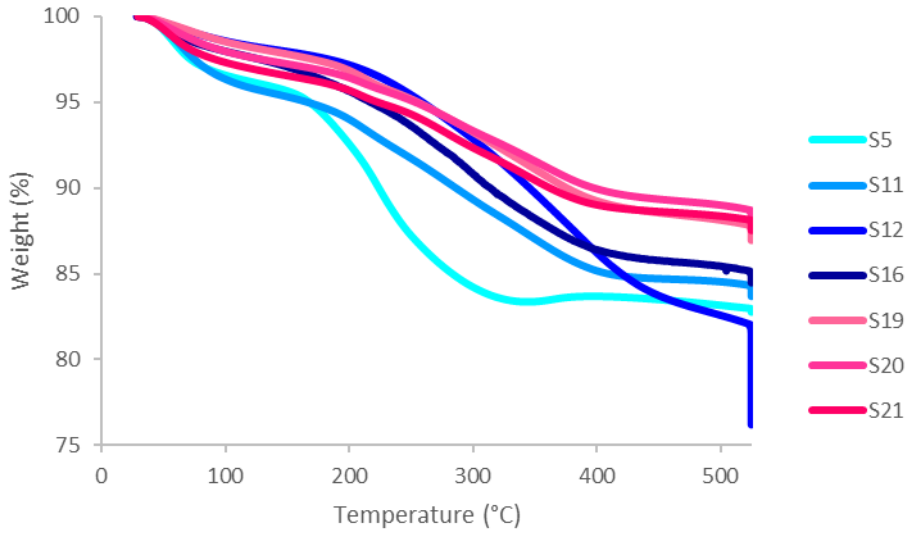

Figure 5.2. *Thermograms of the sample subset selected for magnetics measurements.*

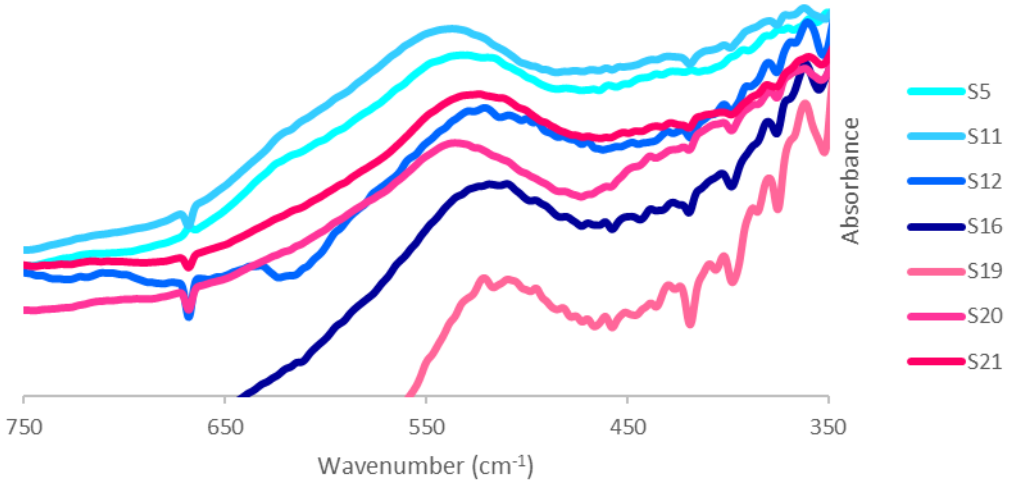

Figure 5.3. *Overlaid IR spectra of the sample subset selected for magnetics measurements.*

5.2 Magnetics Measurements

M_S is the maximum magnetization a material will exhibit in the presence of an increasing external magnetic field, beyond which the moment is considered saturated. The distribution of cations among tetrahedral and octahedral sites influences M_S of the material, where oxygen exchange interactions with cations influences both the sign and magnitude of M_S. Magnetization tends to decrease with particle size, due to the increasing surface contribution at smaller sizes.[103] However, PCA did not identify any clear association of crystallite size with significant sample variance (Figures 4.3, 4.4).

M_S was measured to better understand how the magnetization of the particles could be influenced by synthetic condition, and to which degree it may be associated with particle size and cation occupancy. Figure 5.4 shows the $M(H)$ curves for the samples in the subset, where M is the magnetization of the material and H is the external magnetic field. Characteristic of superparamagnetic materials, hysteresis was not observed for any sample. A negative correlation was observed between the mass percent of TEG surface coating and M_S, as the exterior coating produced a magnetically dead layer around the particles (Figure 3.1). Stir rate had no impact on M_S, while a positive increase in M_S was observed with the addition of a dwell.

It was possible to alter the cation occupancies of the nanoparticles through synthetic modifications without compromising the general form of the nanoparticles (phase, crystallinity, quantity of TEG coating). However, it was determined that synthetic route plays the greatest role in influencing magnetic properties of the material. As seen in Table 5.2, there is no clear trend between v_1 and M_S values.

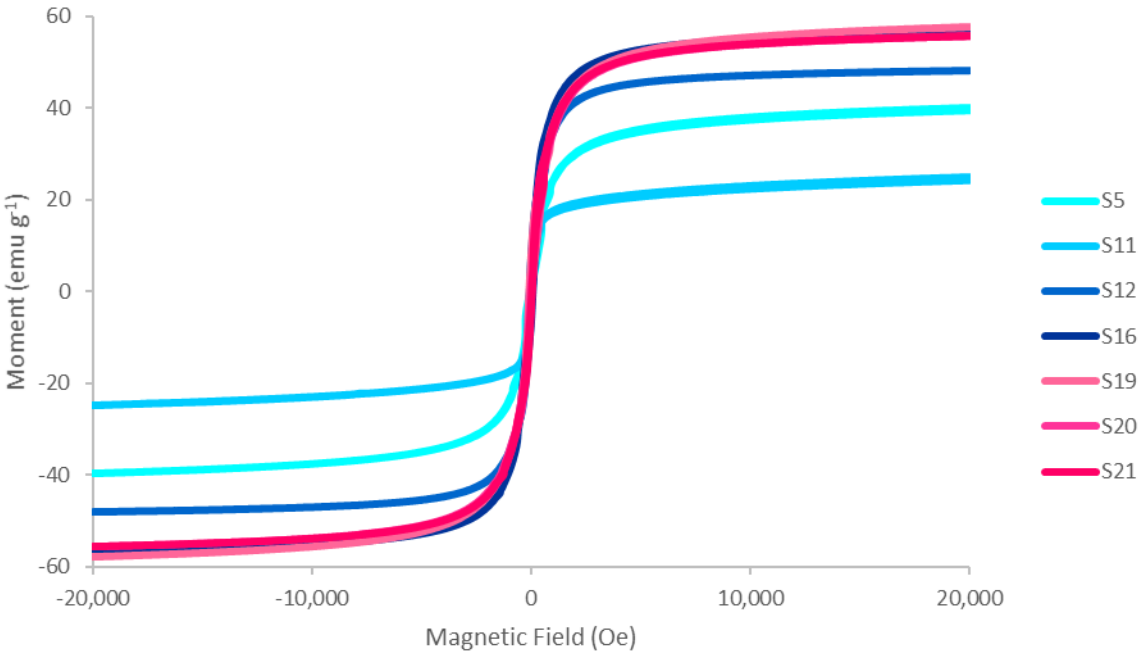

Figure 5.4. *Overlaid M_S measurements for the selected subset.*

Table 5.2. *v_1 Peak Positions and M_S Values for Selected Samples*

Sample ID	v_1 (cm^{-1})	Mn^{2+} octahedral occupancy (%)	M_S (emu g^{-1})
S5	533	0.15	40.12
S11	537	3.27	25.07
S12	521	-8.53	48.16
S16	510	-16.17	56.57
S19	521	-8.18	57.75
S20	536	2.58	55.69
S21	524	-6.45	55.60

Four samples produced similar M_S values larger than 50 emu g^{-1}; all were synthesized with a dwell, were sized between 7 and 9 nm, with only one sample achieving a positive octahedral site occupancy for Mn^{2+}. It can be reasoned that Mn^{2+} presence in octahedral sites has little influence on M_S. Considering these results, it can be seen that in order to maximize M_S for MFO nanoparticles synthesized through the polyol route, specific synthetic steps must be utilized. The synthetic scheme outlined in this work provide a standard for maximizing M_S through the polyol route. Results further indicate that, at least under the size constraints of a nanoparticulate system, controlling for cation occupancy may not be necessary when controlling for magnetic moment.

As thermal energy decreases, the magnetic moment of the particle becomes blocked. At a certain temperature, the preferred direction of magnetization is lost and superparamagnetism is no longer observed. This temperature is referred to as the blocking temperature T_B

$$T_B = \frac{KV}{k_B \ln\left(\frac{\tau_m}{\tau_0}\right)} \tag{5.1}$$

where K is the magnetic anisotropy energy density of the nanoparticle, V is the volume of the nanoparticle, k_B is the Boltzmann constant, and τ_0 is the attempt period for the material. Below T_B, the material exhibits relaxed magnetism. Below T_b, the magnetic properties of the superparamagnetic material are comparable to those of the bulk one.[33]

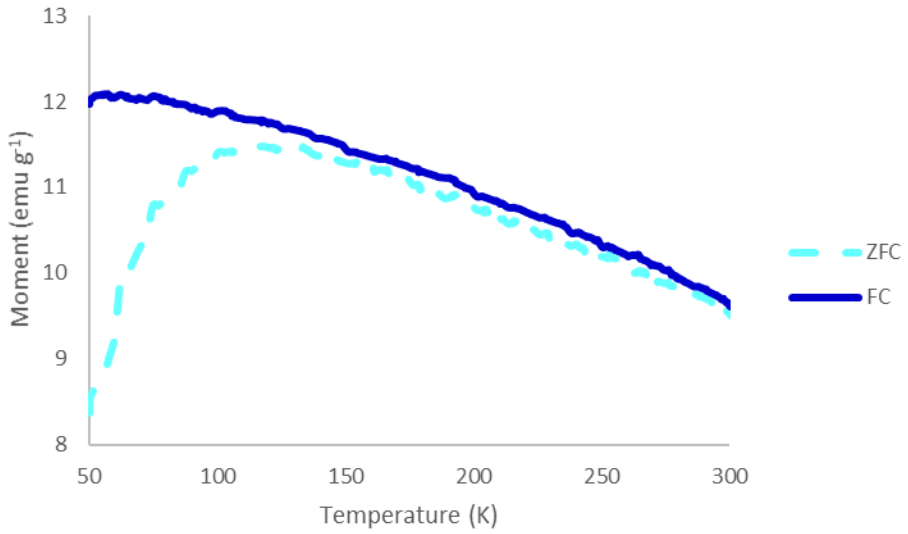

Figure 5.5. *FC and ZFC curves for sample S11.*

Figures 5.5-5.9 shows the overlaid FC and ZFC curves for all samples in the subset, where temperature in K is given on the *x*-axis and magnetic moment in emu g^{-1} is on the *y*-axis. Sample S11, shown in Figure 5.5, shows maximum of the ZFC curve occurring at approximately 100 K. The FC and ZFC curves do not appear to overlap, indicating a large spread of domain sizes. This could explain the low M_S value for sample S11 of 25.07 emu g^{-1}.

Figure 5.6 provides the FC and ZFC curves for sample S12, with T_b occurring around 75 K. The two curves overlap around 125 K, indicating a slight distribution of domain sizes. M_S increased relative to sample S11, up to 48.16 emu g^{-1}.

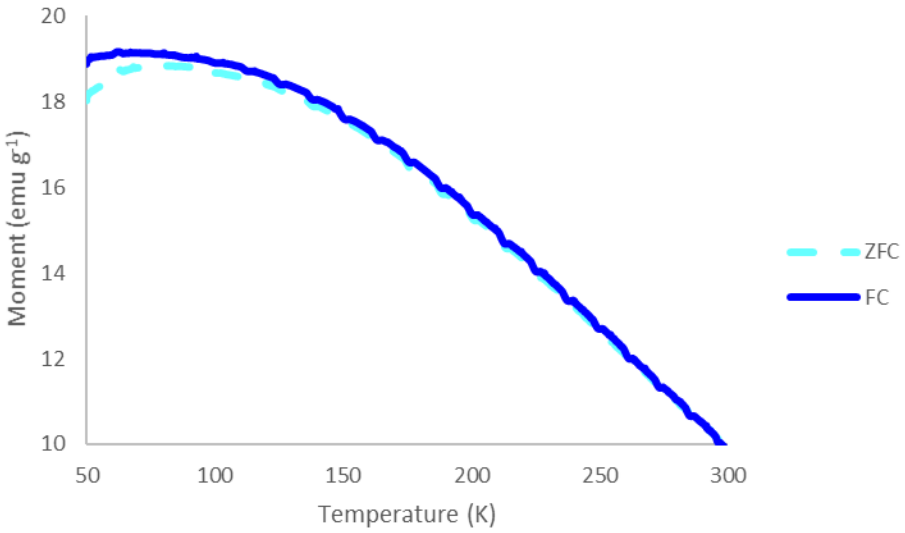

Figure 5.6. *FC and ZFC curves for sample S12.*

The FC and ZFC curves for sample S16 are provided in Figure 5.7, with T_b occurring at 122 K. The two curves overlap at 80 K, which may be the result of to sample movement during measurements. M_S for sample S16 was 56.57 emu g^{-1}, where the decrease in stir rate relative to either samples S11 or S12 appears to have positively impacted saturation values. It was additionally noteworthy that sample S16 was synthesized at a lower solid concentration than S12, but produced an almost 10 emu g^{-1} increase in M_S.

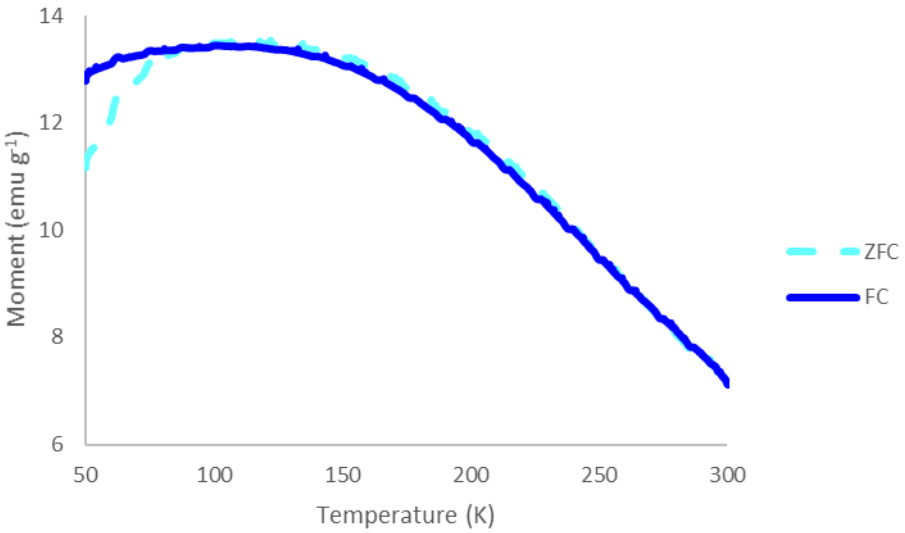

Figure 5.7. *FC and ZFC curves for sample S16.*

Figure 5.8 displays the FC and ZFC curves for sample S19. T_b occurs at 90 K, and the FC and ZFC curves overlap at nearly the same temperature, indicating a narrow distribution of domain sizes. M_S was maximized for sample S19 at 57.75 emu g^{-1}. It should be noted that the synthetic conditions for samples S16 and S19 were identical, though sample S19 produced a v_1 peak maximum 11 cm^{-1} higher than S16. This, combined with the data presented in Figures 5.7 and 5.8, shows that while control has been achieved for this synthetic technique, variability still occurs between individual trials.

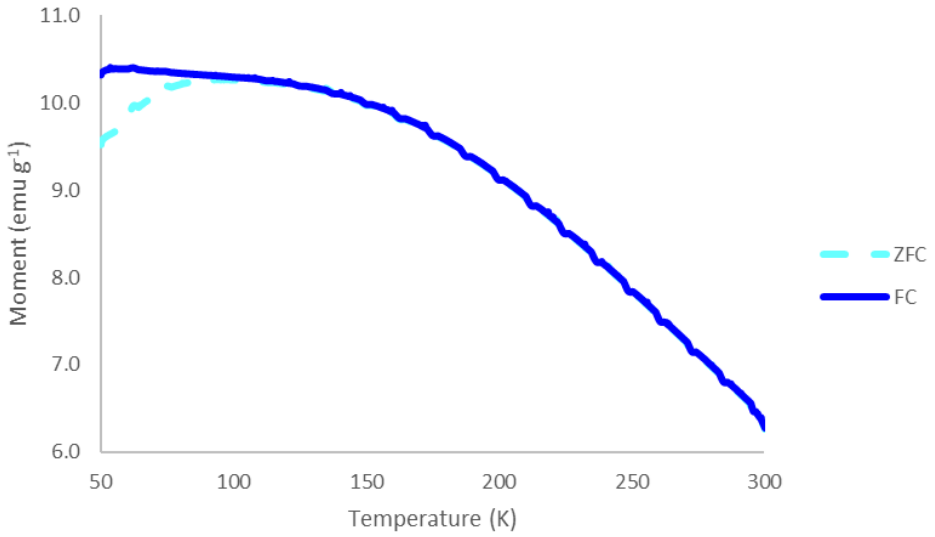

Figure 5.8. *FC and ZFC curves for sample S19.*

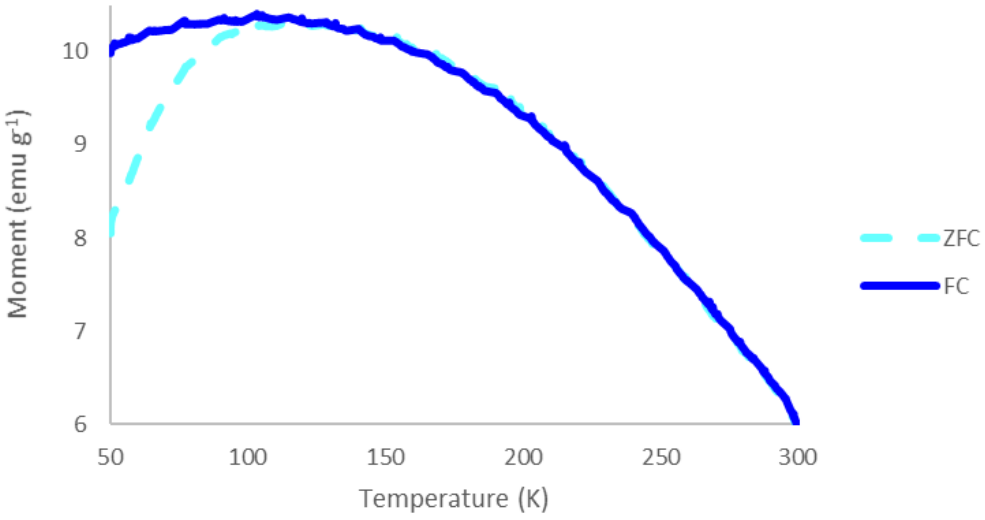

Figure 5.9. *FC and ZFC curves for sample S20.*

FC and ZFC curves for sample S20 are given in Figure 5.9. The maximum of the ZFC occurs at 115 K, while the curves intersect at approximately 140 K. Again, this is indicative of multiple domain sizes for the material. The M_S for sample S20 was only slightly lower than that of sample S19, at 55.69 emu g^{-1}.

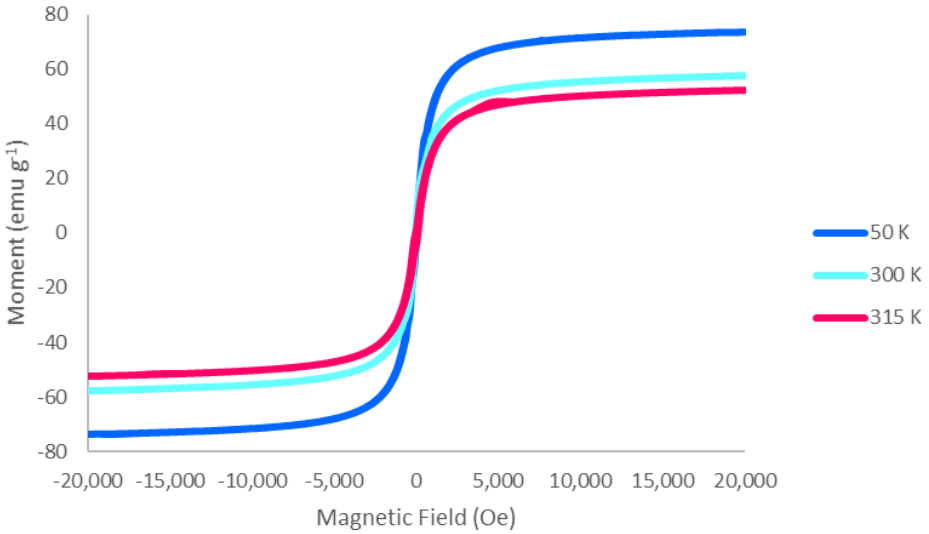

Figure 5.10. *Overlaid M(H) curves for sample S19 at 50 K, 300 K, and 315 K.*

All values of T_b occurred at 100 ± 19 K, well below room temperature and confirmation that all samples fell within the superparamagnetic regime. Deviations between the FC and ZFC curves are indicative of multiple phases present in the sample. T_b was maximized for sample S16 and minimized for sample S12, while sample S11 showed the greatest distance between FC and ZFC curves. Samples S16 and S19 were synthesized under identical conditions, but had different values for v_1. A comparison of $M(T)$ plots supports the increased presence of Mn^{3+} in sample S16, as there is a slightly greater difference between FC and ZFC curves than for sample S19. These results are indicative that there still exists a lack of consistency between identical syntheses that may be due to subtle differences in physical or chemical environment. Generally, it appears that lower concentrations encouraged the presence of multiple phases.

Additional $M(H)$ curves were obtained for a range of temperatures. M_S tends to be inversely proportional to temperature, seen in Figure 5.6. A comparison at 50, 300, and 315 K is shown, with M_S being maximized for sample S19 at 50 K (blue line) and 73.79 emu g^{-1}. M_S was minimized at 315 K (pink line) and 52.55 emu g^{-1}. This brings us into the clinical temperature range for MH, where saturation decreases slightly from that at room temperature.

Table 5.3. *Blocking Temperatures for Selected Samples*

Sample ID	T_b (K)
S11	100
S12	75
S16	122
S19	90
S20	115

Table 5.4. *M_S Values for Sample S19 at Various Temperatures*

Temperature (K)	M_S (emu g^{-1})
50	73.79
300	57.75
315	52.55

T_b was measured as a function of field strength, shown in Figure 5.11 with T_b values given in Table 5.5. As field strength increased from 100 to 1,000 Oe, T_b decreased from 90 to 54 K. Magnetic moment can be seen to be directly proportional with temperature. From the theory surrounding eq. 1.5, it is known that the maximum tolerable field strength for clinical applications is approximately 600 Oe. At 500 Oe, sample S19 has a blocking temperature well below room, maintaining the required superparamagnetic state for MH.

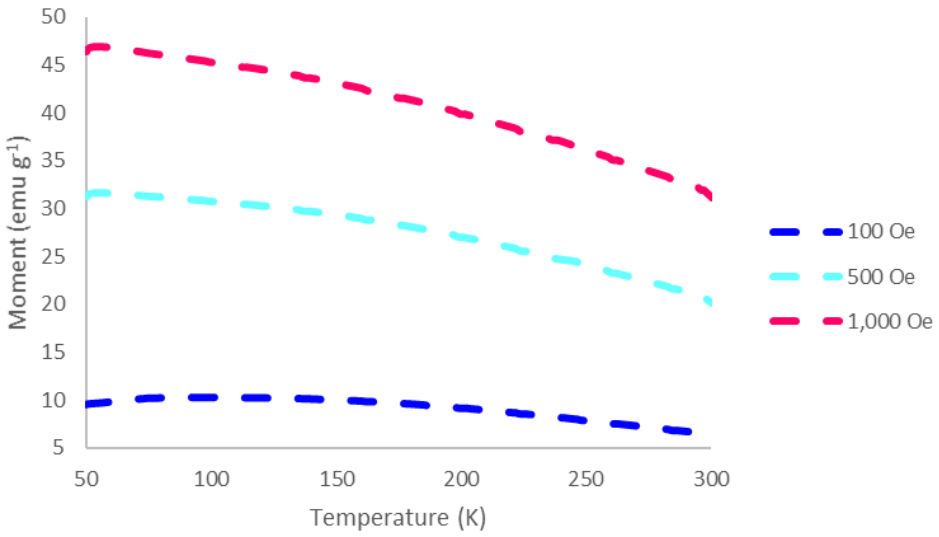

Figure 5.11. *Overlaid ZFC curves for sample S19 at 100 Oe, 500 Oe, and 1,000 Oe.*

Table 5.5. *T_b Values by Field Strength*

Field strength (Oe)	T_b (K)
100	90
500	54
1,000	45

All magnetic characterization maintains that sample S19 is a reasonable candidate for MH applications. Despite the reduced M_S observed in Figure 5.10 at the target temperature range, S19 outperforms similarly sized particles from the literature (11 nm MFO particle with M_S reported at 48 emu g^{-1}, 29 nm MFO particle with M_S reported at 64.26 emu g^{-1}).[36,75] Particularly for the 29 nm particle, at more than 3 times the size of S19, M_S is less than 10 emu g^{-1} greater. This imparts the conclusion that synthetic condition is more influential than material properties when identifying how to target M_S. From Figure 4.8, the T^2 contributions for sample S19 are mainly attributed to TEG volume and stir rate, with a small contribution from dwell time, identifying clear synthetic targets for future studies.

Chapter 6. Conclusions and Future Work

6.1 Conclusions

The goal of this work was to identify which synthetic and material properties could be tailored to best maximize M_S for MH applications. This was accomplished through varying the synthetic conditions of a thermal decomposition and using statistical modeling to identify variables of significant influence. Three synthetic conditions were identified as contributing to the observed variance among samples: solvent volume, stir rate, and dwell time. All material candidates in the statistical model fell below the critical size for superparamagnetism in MFO and had narrow size and shape distributions, essential components of a MH candidate.

M_S was maximized at 57.75 emu g^{-1} under synthetic conditions of 20 mL solvent, stir rate of 500 rpm, and a dwell time of 120 minutes. There was no observable correlation between particle size and M_S for nanoparticles within a size range of 7-12 nm. M_S was found to be insensitive to Mn^{2+} occupancy in octahedral lattice sites for the test set. It can be concluded that a maximal M_S can be achieved irrespective of targeting size or cation distribution, and is instead primarily dependent upon synthetic conditions. Trial-and-error synthesis, specifically at the nanoscale, fails to identify many confounding variables, where the identification of such is critical to enabling MH as a standalone treatment modality. These results not only identify a clear synthetic route when using a thermal decomposition, but provide a new perspective when assessing MH literature at large.

6.2 Future Work

This exploratory work identified the importance of understanding the role those synthetic modifications can impart on nanoparticle properties, particularly when trying to optimize for a specific application. While the understanding that size is the controlling factor in maximizing M_S was not found to hold up under the influence of broad synthetic conditions, the identification of the optimal synthetic parameters when conducting a thermal decomposition may now serve as the blueprint for fine-tuning future studies. The proposed synthetic scheme offers high M_S while minimizing the presence of multiple phases.

Because all crystallite sizes were below the critical size for superparamagnetism, future work may include specific tailoring of particle size through the refined synthetic parameters. Additionally, while cation occupancy showed little dependence on maximizing M_S, the presence of mixed-phase materials may have skewed that understanding. With the identification of key synthetic parameters, it is now possible to more effectively study the influence of size and cation occupancy on M_S, and subsequently SAR. Relaxation mechanisms for heat generation may be temperature dependent, and serve as a next target for material optimization.[104] Cation

distribution has been found to impact Néel temperature, and serves as a logical next target for this work.[105] Additionally, the next variable in the SAR equation worth investigating is frequency, where magnetization may further be influenced.[106] Finally, the proposed material will be ready for *in vivo* studies, which may finally offer a deterministic model of how to realize MH clinically.

References

(1) Cancer https://www.who.int/news-room/fact-sheets/detail/cancer.

(2) Salunkhe, A. B.; Khot, V. M.; Pawar, S. H. Magnetic Hyperthermia with Magnetic Nanoparticles: A Status Review. *Curr. Top. Med. Chem.* **2014**, *14* (5), 572–594. https://doi.org/10.2174/1568026614666140118203550.

(3) Di Corato, R.; Espinosa, A.; Lartigue, L.; Tharaud, M.; Chat, S.; Pellegrino, T.; Ménager, C.; Gazeau, F.; Wilhelm, C. Magnetic Hyperthermia Efficiency in the Cellular Environment for Different Nanoparticle Designs. *Biomaterials* **2014**, *35* (24), 6400–6411. https://doi.org/10.1016/j.biomaterials.2014.04.036.

(4) Cherukuri, P.; Glazer, E. S.; Curley, S. A. Targeted Hyperthermia Using Metal Nanoparticles. *Adv. Drug Deliv. Rev.* **2010**, *62* (3), 339–345. https://doi.org/10.1016/j.addr.2009.11.006.

(5) Fathi Karkan, S.; Mohammadhosseini, M.; Panahi, Y.; Milani, M.; Zarghami, N.; Akbarzadeh, A.; Abasi, E.; Hosseini, A.; Davaran, S. Magnetic Nanoparticles in Cancer Diagnosis and Treatment: A Review. *Artif. Cells, Nanomedicine Biotechnol.* **2017**, *45* (1), 1–5. https://doi.org/10.3109/21691401.2016.1153483.

(6) Dobson, J. Magnetic Nanoparticles for Drug Delivery. *Drug Dev. Res.* **2006**, *67* (1), 55–60. https://doi.org/10.1201/9781351137263-6.

(7) Kim, H. S.; Lee, D. Y. Nanomedicine in Clinical Photodynamic Therapy for the Treatment of Brain Tumors. *Biomedicines* **2022**, *10* (96), 1–26.

(8) Neumann, A.; Gräfe, K.; von Gladiss, A.; Ahlborg, M.; Behrends, A.; Chen, X.; Schumacher, J.; Blancke Soares, Y.; Friedrich, T.; Wei, H.; Malhorta, A.; Aderhold, E.; Bakenecker, A. C.; Lüdtke-Buzug, K.; Buzug, T. M. Recent Developments in Magnetic Particle Imaging. *J. Magn. Magn. Mater.* **2022**, 169037. https://doi.org/10.1016/j.jmmm.2022.169037.

(9) Lu, Y.; Rivera-Rodriguez, A.; Tay, Z. W.; Hensley, D.; Fung, K. L. B.; Colson, C.; Saayujya, C.; Huynh, Q.; Kabuli, L.; Fellows, B.; Chandrasekharan, P.; Rinaldi, C.; Conolly, S. Combining Magnetic Particle Imaging and Magnetic Fluid Hyperthermia for Localized and Image-Guided Treatment. *Int. J. Hyperth.* **2020**, *37* (3), 141–154. https://doi.org/10.1080/02656736.2020.1853252.

(10) Belyanina, I.; Kolovskaya, O.; Zamay, S.; Gargaun, A.; Zamay, T.; Kichkailo, A. Targeted Magnetic Nanotheranostics of Cancer. *Molecules* **2017**, *22* (6), 1–19. https://doi.org/10.3390/molecules22060975.

(11) Lartigue, L.; Innocenti, C.; Kalaivani, T.; Awwad, A.; Sanchez Duque, M. D. M.; Guari, Y.; Larionova, J.; Gueírin, C.; Montero, J. L. G.; Barragan-Montero, V.; Arosio, P.; Lascialfari, A.; Gatteschi, D.; Sangregorio, C. Water-Dispersible Sugar-Coated Iron Oxide Nanoparticles. An Evaluation of Their Relaxometric and Magnetic Hyperthermia Properties. *J. Am. Chem. Soc.* **2011**, *133* (27), 10459–10472. https://doi.org/10.1021/ja111448t.

(12) Chang, D.; Lim, M.; Goos, J. A. C. M.; Qiao, R.; Ng, Y. Y.; Mansfeld, F. M.; Jackson, M.; Davis, T. P.; Kavallaris, M. Biologically Targeted Magnetic Hyperthermia: Potential and Limitations. *Front. Pharmacol.* **2018**, *9* (831), 1–20. https://doi.org/10.3389/fphar.2018.00831.

(13) Johannsen, M.; Thiesen, B.; Wust, P.; Jordan, A. Magnetic Nanoparticle Hyperthermia for Prostate Cancer. *Int. J. Hyperth.* **2010**, *26* (8), 790–795. https://doi.org/10.3109/02656731003745740.

(14) Caizer, C. Optimization Study on Specific Loss Power in Superparamagnetic Hyperthermia with Magnetite Nanoparticles for High Efficiency in Alternative Cancer Therapy. *Nanomaterials* **2021**, *11* (40), 1–20.

(15) Tay, Z. W.; Chandrasekharan, P.; Chiu-Lam, A.; Hensley, D. W.; Dhavalikar, R.; Zhou, X. Y.; Yu, E. Y.; Goodwill, P. W.; Zheng, B.; Rinaldi, C.; Conolly, S. M. Magnetic Particle Imaging-Guided Heating in Vivo Using Gradient Fields for Arbitrary Localization of Magnetic Hyperthermia Therapy. *ACS Nano* **2018**, *12* (4), 3699–3713. https://doi.org/10.1021/acsnano.8b00893.

(16) Ling, Y.; Tang, X.; Wang, F.; Zhou, X.; Wang, R.; Deng, L.; Shang, T.; Liang, B.; Li, P.; Ran, H.; Wang, Z.; Hu, B.; Li, C.; Zuo, G.; Zheng, Y. Highly Efficient Magnetic Hyperthermia Ablation of Tumors Using Injectable Polymethylmethacrylate-Fe3O4. *RSC Adv.* **2017**, *7* (5), 2913–2918. https://doi.org/10.1039/c6ra20860f.

(17) Capistrano, G.; Rodrigues, H. F.; Zufelato, N.; Gonçalves, C.; Cardoso, C. G.; Silveira-Lacerda, E. P.; Bakuzis, A. F. Noninvasive Intratumoral Thermal Dose Determination during in Vivo Magnetic Nanoparticle Hyperthermia: Combining Surface Temperature Measurements and Computer Simulations. *Int. J. Hyperth.* **2020**, *37* (3), 120–140. https://doi.org/10.1080/02656736.2020.1826583.

(18) Niculaes, D.; Lak, A.; Anyfantis, G. C.; Marras, S.; Laslett, O.; Avugadda, S. K.; Cassani, M.; Serantes, D.; Hovorka, O.; Chantrell, R.; Pellegrino, T. Asymmetric Assembling of Iron Oxide Nanocubes for Improving Magnetic Hyperthermia Performance. *ACS Nano* **2017**, *11* (12), 12121–12133. https://doi.org/10.1021/acsnano.7b05182.

(19) Yan, H.; Shang, W.; Sun, X.; Zhao, L.; Wang, J.; Xiong, Z.; Yuan, J.; Zhang, R.; Huang, Q.; Wang, K.; Li, B.; Tian, J.; Kang, F.; Feng, S. S. "All-in-One" Nanoparticles for Trimodality Imaging-Guided Intracellular Photo-Magnetic Hyperthermia Therapy under Intravenous Administration. *Adv. Funct. Mater.* **2018**, *28* (9), 1–12. https://doi.org/10.1002/adfm.201705710.

(20) Ovejero, J. G.; Serantes, D.; Veintemillas-verdaguer, S.; Zeballos, N.; Fuente, M. De; Morales, P.; Fernando, L.; Gru, C.; Grazu, V. Selective Magnetic Nanoheating: Combining Iron Oxide Nanoparticles for Multi-Hot-Spot Induction and Sequential Regulation. *Nano Lett.* **2021**, *21* (17), 7213–7220. https://doi.org/10.1021/acs.nanolett.1c02178.

(21) Liu, X. L.; Choo, E. S. G.; Ahmed, A. S.; Zhao, L. Y.; Yang, Y.; Ramanujan, R. V.; Xue, J. M.; Fan, D. Di; Fan, H. M.; Ding, J. Magnetic Nanoparticle-Loaded Polymer Nanospheres as Magnetic Hyperthermia Agents. *J. Mater. Chem. B* **2014**, *2* (1), 120–128. https://doi.org/10.1039/c3tb21146k.

(22) Feddersen, T. V; Hernandez-tamames, J. A.; Franckena, M.; Rhoon, G. C. Van; Paulides, M. M. Clinical Performance and Future Potential of Magnetic Resonance Thermometry in Hyperthermia. *Cancers (Basel).* **2021**, *13* (31), 1–19.

(23) Espinosa, A.; Castro, G. R.; Reguera, J.; Castellano, C.; Castillo, J.; Camarero, J.; Wilhelm, C.; Angel, M.; Mun, A. Photoactivated Nanoscale Temperature Gradient Detection Using X - Ray Absorption Spectroscopy as a Direct Nanothermometry Method. *Nano Lett.* **2020**. https://doi.org/10.1021/acs.nanolett.0c04477.

(24) Dutz, S.; Hergt, R. Magnetic Particle Hyperthermia - A Promising Tumour Therapy? *Nanotechnology* **2014**, *25* (45), 1–28. https://doi.org/10.1088/0957-4484/25/45/452001.

(25) Zheng, Y.; Lin, Y.; Yang, D. Hyperthermia : A Cancer Treatment Approach Worth More Attention. *J. Res. Clin. Oncol.* **2021**, *1* (1), 1–5.

(26) Hergt, R.; Dutz, S. Magnetic Particle Hyperthermia-Biophysical Limitations of a Visionary Tumour Therapy. *J. Magn. Magn. Mater.* **2007**, *311* (1 SPEC. ISS.), 187–192. https://doi.org/10.1016/j.jmmm.2006.10.1156.

(27) Toropova, Y.; Istomina, M.; Shulmeyster, G.; Petukhov, A.; Mishanin, V.; Gorshkov, A.; Podyacheva, E.; Demidov, O. Controlling the Movement of Magnetic Iron Oxide Nanoparticles Intended for Targeted Delivery of Cytostatics. *Int. J. Nanomedicine* **2021**, *20* (16), 5651–5664.

(28) Mehdaoui, B.; Tan, R. P.; Meffre, A.; Carrey, J.; Lachaize, S.; Chaudret, B.; Respaud, M. Increase of Magnetic Hyperthermia Efficiency Due to Dipolar Interactions in Low-Anisotropy Magnetic Nanoparticles: Theoretical and Experimental Results. *Phys. Rev. B - Condens. Matter Mater. Phys.* **2013**, *87* (17), 1–10. https://doi.org/10.1103/PhysRevB.87.174419.

(29) O'Reilly, E. P. Diamagnetism and Paramagnetism. *Quantum Theory of Solids* **2010**, 128–146. https://doi.org/10.4324/9780203212158_chapter_6.

(30) Morrish, A. H. *The Physical Principles of Magnetism*; 2001. https://doi.org/10.1109/9780470546581.

(31) Kim, J.; Piao, Y.; Hyeon, T. Multifunctional Nanostructured Materials for Multimodal Imaging, and Simultaneous

Imaging and Therapy. *Chem. Soc. Rev.* **2009**, *38* (2), 372–390. https://doi.org/10.1039/b709883a.

(32) Gubin, S. P.; Koksharov, Y. A.; Khomutov, G. B.; Yurkov, G. Y. Magnetic Nanoparticles: Preparation, Structure and Properties. *Usp. Khim.* **2005**, *74* (6), 539–574. https://doi.org/10.1070/rc2005v074n06abeh000897.

(33) Concas, G.; Congiu, F.; Muscas, G.; Peddis, D. Determination of Blocking Temperature in Magnetization and Mössbauer Time Scale: A Functional Form Approach. *J. Phys. Chem. C* **2017**, *121* (30), 16541–16548. https://doi.org/10.1021/acs.jpcc.7b01748.

(34) Cho, S. J.; Jarrett, B. R.; Louie, A. Y.; Kauzlarich, S. M. Gold-Coated Iron Nanoparticles: A Novel Magnetic Resonance Agent for T 1 and T2 Weighted Imaging. *Nanotechnology* **2006**, *17* (3), 640–644. https://doi.org/10.1088/0957-4484/17/3/004.

(35) Phong, P. T.; Nguyen, L. H.; Manh, D. H.; Lee, I. J.; Phuc, N. X. Computer Simulations of Contributions of Néel and Brown Relaxation to Specific Loss Power of Magnetic Fluids in Hyperthermia. *J. Electron. Mater.* **2017**, *46* (4), 2393–2405. https://doi.org/10.1007/s11664-017-5302-6.

(36) Nguyen, L. H.; Phuc, N. X.; Manh, D. H.; Nam, N. H.; Truong, N. X.; Quynh, N. V.; Phong, P. T.; Nam, P. H. Size-Dependent Magnetic Heating of MnFe2O4 Nanoparticles. *J. Electron. Mater.* **2021**, *50*, 5318–5326. https://doi.org/10.1007/s11664-021-09056-7.

(37) Mukhopadhyay, A.; Joshi, N.; Chattopadhyay, K.; De, G. A Facile Synthesis of PEG-Coated Magnetite (Fe 3O 4) Nanoparticles and Their Prevention of the Reduction of Cytochrome C. *ACS Appl. Mater. Interfaces* **2012**, *4* (1), 142–149. https://doi.org/10.1021/am201166m.

(38) Sadat, M. E.; Patel, R.; Sookoor, J.; Bud'Ko, S. L.; Ewing, R. C.; Zhang, J.; Xu, H.; Wang, Y.; Pauletti, G. M.; Mast, D. B.; Shi, D. Effect of Spatial Confinement on Magnetic Hyperthermia via Dipolar Interactions in Fe3O4 Nanoparticles for Biomedical Applications. *Mater. Sci. Eng. C* **2014**, *42*, 52–63. https://doi.org/10.1016/j.msec.2014.04.064.

(39) Guardia, P.; Di Corato, R.; Lartigue, L.; Wilhelm, C.; Espinosa, A.; Garcia-Hernandez, M.; Gazeau, F.; Manna, L.; Pellegrino, T. Water-Soluble Iron Oxide Nanocubes with High Values of Specific Absorption Rate for Cancer Cell Hyperthermia Treatment. *ACS Nano* **2012**, *6* (4), 3080–3091. https://doi.org/10.1021/nn2048137.

(40) Gennaro G. Bellizzi, Kemal Sumer, M. T. B. O Ptimal M Ultiperiod a Sset a Llocation : M Atching. *IEEE J. Electromagn. RF Microwaves Med. Biol.* **2010**, *77* (2), 451–472. https://doi.org/10.1109/JERM.2020.3047980.

(41) Mahmood, H. S.; Mubarak, T. H.; Ali Ridha, S. M.; Al-Zanganawee, J. Effect of Zinc Substitution in Magnetite Structure on Heat Efficiency for Hyperthermia : Investigation in Superparamagnetic Properties. **2022**, *070006*.

(42) Nikolovski, D.; Jeremic, M.; Paunovic, J.; Vucevic, D.; Radosavljevic, T.; Radojevi-Škodri, S.; Rakocevic, R.; Nesic, D.; Pantic, I. Application of Iron Oxide Nanoparticles in Contemporary Experimental Physiology and Cell Biology Research. *Rev. Adv. Mater. Sci.* **2018**, *53* (1), 74–78. https://doi.org/10.1515/rams-2018-0005.

(43) Fortin, J. P.; Wilhelm, C.; Servais, J.; Ménager, C.; Bacri, J. C.; Gazeau, F. Size-Sorted Anionic Iron Oxide Nanomagnets as Colloidal Mediators for Magnetic Hyperthermia. *J. Am. Chem. Soc.* **2007**, *129* (9), 2628–2635. https://doi.org/10.1021/ja067457e.

(44) Tran, H.; Ngo, N. M.; Medhi, R.; Srinoi, P.; Liu, T.; Rittikulsittichai, S.; Lee, T. R. Multifunctional Iron Oxide Magnetic Nanoparticles for Biomedical Applications : A Review. *Materials (Basel).* **2022**, *15* (2), 503.

(45) Lee, J. H.; Kim, B.; Kim, Y.; Kim, S. K. Ultra-High Rate of Temperature Increment from Superparamagnetic Nanoparticles for Highly Efficient Hyperthermia. *Sci. Rep.* **2021**, *11* (1), 1–9. https://doi.org/10.1038/s41598-021-84424-1.

(46) Wu, X.; Zhang, H. Therapeutic Strategies of Iron-Based Nanomaterials for Cancer Therapy. *Biomed. Mater.* **2021**, *16* (032003), 1–16.

(47) Klekotka, U.; Satuła, D.; Spassov, S.; Kalska-Szostko, B. Influence of Atomic Doping on Thermal Stability of Ferrite

Nanoparticles-Structural and Magnetic Studies. *Materials (Basel).* **2021**, *14* (100), 1–15.

(48) Bhandare, S. V.; Kumar, R.; Anupama, A. V.; Choudhary, H. K.; Jali, V. M.; Sahoo, B. Annealing Temperature Dependent Structural and Magnetic Properties of MnFe2O4 Nanoparticles Grown by Sol-Gel Auto-Combustion Method. *J. Magn. Magn. Mater.* **2017**, *433*, 29–34. https://doi.org/10.1016/j.jmmm.2017.02.040.

(49) Shin, S. W.; Yang, K.; Lee, M.; Moon, J.; Son, A.; Kim, Y.; Choi, S.; Kim, D. H.; Choi, C.; Lee, N.; Park, H. C. Manganese Ferrite Nanoparticles Enhance the Sensitivity of Hepa1-6 Hepatocellular Carcinoma to Radiation by Remodeling Tumor Microenvironments. *Int. J. Mol. Sci.* **2021**, *22* (5), 1–15. https://doi.org/10.3390/ijms22052637.

(50) Ma, Y.; Xu, X.; Lu, L.; Meng, K.; Wu, Y.; Chen, J.; Miao, J.; Jiang, Y. Facile Synthesis of Ultrasmall MnFe2O4 Nanoparticles with High Saturation Magnetization for Magnetic Resonance Imaging. *Ceram. Int.* **2021**, *47* (24), 34005–34011. https://doi.org/10.1016/j.ceramint.2021.08.308.

(51) Ibrahim, M.; Abdel, A.; Ghobashy, M. M.; Kodous, A. S.; Fahim, R. A.; Osman, A. I.; Muhtaseb, H. Al; Rooney, D. W.; Mamdouh, M. A.; Nady, N.; Ashour, A. H. Insights on Magnetic Spinel Ferrites for Targeted Drug Delivery and Hyperthermia Applications. *Nanotech* **2022**, *11* (1), 372–413.

(52) Pham, T. N.; Huy, T. Q.; Le, A. T. Spinel Ferrite (AFe2O4)-Based Heterostructured Designs for Lithium-Ion Battery, Environmental Monitoring, and Biomedical Applications. *RSC Adv.* **2020**, *10* (52), 31622–31661. https://doi.org/10.1039/d0ra05133k.

(53) Miessler, G. L.; Fischer, P. J.; Tarr, D. A. Inorganic Chemistry, Fifth Edition. In *Inorganic Chemistry*; Pearson, 2014; pp 215–249.

(54) Sanchez-Lievanos, K. R.; Stair, J. L.; Knowles, K. E. Cation Distribution in Spinel Ferrite Nanocrystals: Characterization, Impact on Their Physical Properties, and Opportunities for Synthetic Control. *Inorg. Chem.* **2021**, *60* (7), 4291–4305. https://doi.org/10.1021/acs.inorgchem.1c00040.

(55) Xie, X.; Wang, B.; Wang, Y.; Ni, C.; Sun, X.; Du, W. MFe2O4 (M = Fe, Co, Ni, Mn, Zn) and Their Composites for Microwave Absorption: A Review. *Chem. Eng. J.* **2022**, *428*, 1–19. https://doi.org/10.1016/j.cej.2021.131160.

(56) Huang, J. R.; Cheng, C. Cation and Magnetic Orders in MnFe2O4 from Density Functional Calculations. *J. Appl. Phys.* **2013**, *113* (3), 033912. https://doi.org/10.1063/1.4776771.

(57) Talebniya, S.; Sharifi, I.; Saeri, M. R.; Doostmohammadi, A. Study of Cation Distribution and Magnetic Properties of MFe2O4 (M = Fe, Co, Zn, Mn, and Cu) Nanoparticles. *J. Supercond. Nov. Magn.* **2022**, *4* (0123456789). https://doi.org/10.1007/s10948-021-06129-w.

(58) Usov, N. A.; Rytov, R. A.; Bautin, V. A. Properties of Assembly of Superparamagnetic Nanoparticles in Viscous Liquid. *Sci. Rep.* **2020**, *11* (1), 6999.

(59) Jiang, L.; Li, X.; Liu, L.; Zhang, Q. Thiolated Chitosan-Modified PLA-PCL-TPGS Nanoparticles for Oral Chemotherapy of Lung Cancer. *Nanoscale Res. Lett.* **2013**, *8* (1), 1–12. https://doi.org/10.1186/1556-276X-8-66.

(60) Cervadoro, A.; Giverso, C.; Pande, R.; Sarangi, S.; Preziosi, L.; Wosik, J.; Brazdeikis, A.; Decuzzi, P. Design Maps for the Hyperthermic Treatment of Tumors with Superparamagnetic Nanoparticles. *PLoS One* **2013**, *8* (2), 1–14. https://doi.org/10.1371/journal.pone.0057332.

(61) Akbarzadeh, A.; Samiei, M.; Davaran, S. Magnetic Nanoparticles: Preparation, Physical Properties, and Applications in Biomedicine. *Nanoscale Res. Lett.* **2012**, *7* (144), 1–13. https://doi.org/10.1016/j.jmig.2015.01.027.

(62) Kim, D. H.; Kim, K. N.; Kim, K. M.; Lee, Y. K. Targeting to Carcinoma Cells with Chitosan- and Starch-Coated Magnetic Nanoparticles for Magnetic Hyperthermia. *J. Biomed. Mater. Res. - Part A* **2008**, *88* (1), 1–11. https://doi.org/10.1002/jbm.a.31775.

(63) Hayashi, K.; Ono, K.; Suzuki, H.; Sawada, M.; Moriya, M.; Sakamoto, W.; Yogo, T. One-Pot Biofunctionalization of

Magnetic Nanoparticles via Thiol-Ene Click Reaction for Magnetic Hyperthermia and Magnetic Resonance Imaging. *Chem. Mater.* **2010**, *22* (12), 3768–3772. https://doi.org/10.1021/cm100810g.

(64) Samanta, B.; Yan, H.; Fischer, N. O.; Shi, J.; Jerry, D. J.; Rotello, V. M. Protein-Passivated Fe3O4 Nanoparticles: Low Toxicity and Rapid Heating for Thermal Therapy. *J. Mater. Chem.* **2008**, *18* (11), 1204–1208. https://doi.org/10.1039/b718745a.

(65) Ghosh, R.; Pradhan, L.; Devi, Y. P.; Meena, S. S.; Tewari, R.; Kumar, A.; Sharma, S.; Gajbhiye, N. S.; Vatsa, R. K.; Pandey, B. N.; Ningthoujam, R. S. Induction Heating Studies of Fe3O4 Magnetic Nanoparticles Capped with Oleic Acid and Polyethylene Glycol for Hyperthermia. *J. Mater. Chem.* **2011**, *21* (35), 13388–13398. https://doi.org/10.1039/c1jm10092k.

(66) Abdellahi, M.; Tajally, M.; Mirzaee, O. The Effect of the Particle Size on the Heating and Drug Release Potential of the Magnetic Nanoparticles in a Novel Point of View. *J. Magn. Magn. Mater.* **2021**, *530*, 167938. https://doi.org/10.1016/j.jmmm.2021.167938.

(67) Batlle, X.; Moya, C.; Escoda-Torroella, M.; Iglesias, `Oscar; Rodríguez, A. F.; Labarta, A. Magnetic Nanoparticles: From the Nanostructure to the Physical Properties. *J. Magn. Magn. Mater.* **2022**, *543* (September 2021), 1–28. https://doi.org/10.1016/j.jmmm.2021.168594.

(68) Morfin-Gutiérrez, A.; Meléndez-Ortiz, H. I.; Puente-Urbina, B. A.; García-Cerda, L. A. Synthesis of Poly(N-Vinylcaprolactam)-Grafted Magnetite Nanocomposites for Magnetic Hyperthermia. *J. Nanomater.* **2018**, *2018*, 1–6. https://doi.org/10.1155/2018/9562020.

(69) Willard, M. A.; Kurihara, L. K.; Carpenter, E. E.; Calvin, S.; Harris, V. G. Chemically Prepared Magnetic Nanoparticles. *Int. Mater. Rev.* **2004**, *49* (3–4), 125–170. https://doi.org/10.1179/095066004225021882.

(70) Gonzales-weimuller, M.; Zeisberger, M.; Krishnan, K. M. Size-Dependant Heating Rates of Iron Oxide Nanoparticles for Magnetic Fluid Hyperthermia. **2009**, *321*, 1947–1950. https://doi.org/10.1016/j.jmmm.2008.12.017.

(71) Wang, Y.; Xia, Y. Bottom-up and Top-down Approaches to the Synthesis of Monodispersed Spherical Colloids of Low Melting-Point Metals. *Nano Lett.* **2004**, *4* (10), 2047–2050. https://doi.org/10.1021/nl048689j.

(72) Dong, H.; Chen, Y. C.; Feldmann, C. Polyol Synthesis of Nanoparticles: Status and Options Regarding Metals, Oxides, Chalcogenides, and Non-Metal Elements. *Green Chem.* **2015**, *17* (8), 4107–4132. https://doi.org/10.1039/c5gc00943j.

(73) Lickmichand, M.; Shaji, C. S.; Valarmathi, N.; Benjamin, A. S.; Arun Kumar, R. K.; Nayak, S.; Saraswathy, R.; Sumathi, S.; Arunai Nambi Raj, N. In Vitro Biocompatibility and Hyperthermia Studies on Synthesized Cobalt Ferrite Nanoparticles Encapsulated with Polyethylene Glycol for Biomedical Applications. *Mater. Today Proc.* **2019**, *15*, 252–261. https://doi.org/10.1016/j.matpr.2019.05.002.

(74) De Yoreo, J. J. Principles of Crystal Nucleation and Growth. *Rev. Mineral. Geochemistry* **2003**, *54* (1), 57–93. https://doi.org/10.2113/0540057.

(75) Günay, M.; Erdemi, H.; Baykal, A.; Sözeri, H.; Toprak, M. S. Triethylene Glycol Stabilized MnFe2O4 Nanoparticle: Synthesis, Magnetic and Electrical Characterization. *Mater. Res. Bull.* **2013**, *48* (3), 1057–1064. https://doi.org/10.1016/j.materresbull.2012.11.097.

(76) Basina, G.; Tzitzios, V.; Niarchos, D.; Li, W.; Khurshid, H.; Mao, H.; Hadjipanayis, C.; Hadjipanayis, G. Water-Soluble Spinel Ferrites by a Modified Polyol Process as Contrast Agents in MRI. *AIP Conf. Proc.* **2010**, *1311* (December 2010), 441–446. https://doi.org/10.1063/1.3530053.

(77) Cortés-Llanos, B.; Ocampo, S. M.; Cueva, L. de la C.; Calvo, G. F.; Belmonte-Beitia, J.; Lucas, P.; Salas, G.; Ayuso-Sacido, Á. Influence of Coating and Size of Magnetic Nanoparticles on Cellular Uptake for In Vitro MRI. *Nanomaterials* **2021**, *11*, 1–20.

(78) Murase, K.; Oonoki, J.; Takata, H.; Song, R.; Angraini, A.; Ausanai, P.; Matsushita, T. Simulation and Experimental

Studies on Magnetic Hyperthermia with Use of Superparamagnetic Iron Oxide Nanoparticles. *Radiol. Phys. Technol.* **2011**, *4* (2), 194–202. https://doi.org/10.1007/s12194-011-0123-4.

(79) Solano, E.; Yáñez, R.; Ricart, S.; Ros, J. New Approach towards the Polyol Route to Fabricate MFe2O4 Magnetic Nanoparticles: The Use of MCl2 and Fe(Acac)3 as Chemical Precursors. *J. Magn. Magn. Mater.* **2015**, *382*, 380–385. https://doi.org/10.1016/j.jmmm.2015.02.002.

(80) Feldmann, C.; Jungk, H. O. Polyol-Mediated Preparation of Nanoscale Oxide Particles. *Angew. Chemie - Int. Ed.* **2001**, *40* (2), 359–362. https://doi.org/10.1002/1521-3773(20010119)40:2<359::AID-ANIE359>3.0.CO;2-B.

(81) Sun, S.; Zeng, H.; Robinson, D. B.; Raoux, S.; Rice, P. M.; Wang, S. X.; Li, G. Monodisperse MFe 2 O 4 (M) Fe , Co , Mn) Nanoparticles. **2004**, *4* (1), 126–132. https://doi.org/10.1021/ja0380852.

(82) Lee, T.; Lim, E. K.; Lee, J.; Kang, B.; Choi, J.; Park, H. S.; Suh, J. S.; Huh, Y. M.; Haam, S. Efficient CD44-Targeted Magnetic Resonance Imaging (MRI) of Breast Cancer Cells Using Hyaluronic Acid (HA)-Modified MnFe 2 O 4 Nanocrystals. *Nanoscale Res. Lett.* **2013**, *8* (1), 1–9. https://doi.org/10.1186/1556-276X-8-149.

(83) Tang, Y.; Flesch, R. C. C.; Jin, T.; Gao, Y.; He, M. Effect of Nanoparticles Shape on Therapeutic Temperature Distribution during Magnetic Hyperthermia. *J. Phys. D. Appl. Phys.* **2019**, *54*, 165401.

(84) Jain, R. A Review on the Development of XRD in Ferrite Nanoparticles. *J. Supercond. Nov. Magn.* **2022**. https://doi.org/10.1007/s10948-022-06213-9.

(85) Baerlocher, W. I. F. D. K. S. L. B. M. C. *Structure Determination from Powder Diffraction Data*; Oxford University Press, Incorporated, 2002.

(86) Urgast, D. S.; Beattie, J. H.; Feldmann, J. Imaging of Trace Elements in Tissues: With a Focus on Laser Ablation Inductively Coupled Plasma Mass Spectrometry. *Curr. Opin. Clin. Nutr. Metab. Care* **2014**, *17* (5), 431–439. https://doi.org/10.1097/MCO.0000000000000087.

(87) Bottom, R. Thermogravimetric Analysis. *Princ. Appl. Therm. Anal.* **2008**, *1* (906), 87–118. https://doi.org/10.1002/9780470697702.ch3.

(88) Braidy, N.; Béchu, A.; de Souza Terra, J. C.; Patience, G. S. Experimental Methods in Chemical Engineering: Transmission Electron Microscopy—TEM. *Can. J. Chem. Eng.* **2020**, *98* (3), 628–641. https://doi.org/10.1002/cjce.23692.

(89) Man, Y. B. C.; Syahariza, Z. A.; Rohman, A. Fourier Transform Infra-Red (FTIR) Spectroscopy: Development, Techniques, and Application in the Analyses of Fats and Oils. **2020**, 1–26.

(90) Shultz, M. D.; Carpenter, E. E.; Morrison, S. A.; Calvin, S. Cation Occupancy Determination in Manganese Zinc Ferrites Using Fourier Transform Infrared Spectroscopy. *J. Appl. Phys.* **2006**, *99* (8), 2004–2007. https://doi.org/10.1063/1.2151831.

(91) Yu, C.; Fan, J.; Tian, B.; Zhao, D. Morphology Development of Mesoporous Materials: A Colloidal Phase Separation Mechanism. *Chem. Mater.* **2004**, *16* (5), 889–898. https://doi.org/10.1021/cm035011g.

(92) Abdolrahimi, M.; Vasilakaki, M.; Slimani, S.; Ntallis, N.; Varvaro, G.; Laureti, S.; Meneghini, C.; Trohidou, K. N.; Fiorani, D.; Peddis, D. Magnetism of Nanoparticles : Effect of the Organic Coating. *Nanomaterials* **2021**, 1–17.

(93) Ghorai, S.; Ivanov, S. A.; Skini, R.; Svedlindh, P. Evolution of Griffiths Phase and Critical Behaviour of La1-XPbxMnO3 Ysolid Solutions. *J. Phys. Condens. Matter* **2021**, *33* (14). https://doi.org/10.1088/1361-648X/abdd64.

(94) Pramanik, A. K.; Banerjee, A. Griffiths Phase and Its Evolution with Mn-Site Disorder in the Half-Doped Manganite Pr 0.5 Sr 0.5 Mn 1-y Ga y O 3 (Y=0.0, 0.025, and 0.05). *Phys. Rev. B - Condens. Matter Mater. Phys.* **2010**, *81* (2), 1–5. https://doi.org/10.1103/PhysRevB.81.024431.

(95) Mayrhofer, B.; Nývlt, J. Programmed Cooling of Batch Crystallizers. *Chem. Eng. Process.* **1988**, *24* (4), 217–220.

https://doi.org/10.1016/0255-2701(88)85005-0.

(96) Jollife, I. T.; Cadima, J. Principal Component Analysis: A Review and Recent Developments. *Philos. Trans. R. Soc. A* **2016**, *374* (2065), 1–16. https://doi.org/10.1098/rsta.2015.0202.

(97) Lever, J.; Krzywinski, M.; Altman, N. Points of Significance: Principal Component Analysis. *Nat. Methods* **2017**, *14* (7), 641–642. https://doi.org/10.1038/nmeth.4346.

(98) Rodionova, O.; Kucheryavskiy, S.; Pomerantsev, A. Efficient Tools for Principal Component Analysis of Complex Data—a Tutorial. *Chemom. Intell. Lab. Syst.* **2021**, *213*, 104304. https://doi.org/10.1016/j.chemolab.2021.104304.

(99) Beebe, K. R.; Pell, R. J.; Seasholtz, M. B. *Chemometrics: A Practical Guide*, 1st ed.; Wiley-Interscience: New York, NY, 1998.

(100) Hess, K. T.; Ludwig, A.; Pröhl, C.; Schmidt, K. D.; Zocher, M. *Multivariate Methods*; 2016. https://doi.org/10.1007/978-3-319-30056-6_26.

(101) Abdi, H.; Williams, L. J. Principal Component Analysis. *Wiley Interdiscip. Rev. Comput. Stat.* **2010**, *2* (4), 433–459. https://doi.org/10.1002/wics.101.

(102) Abu-Elsaad, N. I.; Nawara, A. S.; Mazen, S. A. Synthesis, Structural Characterization, and Magnetic Properties of Ni–Zn Nanoferrites Substituted with Different Metal Ions (Mn2+, Co2+, and Cu2+). *J. Phys. Chem. Solids* **2020**, *146*, 109620. https://doi.org/10.1016/j.jpcs.2020.109620.

(103) Dyakonov, V.; Lawska-Waniewska, A.; Kazmierczak, J.; Piotrowski, K.; Iesenchuk, O.; Szymczak, H.; Zubov, E.; Myronova, S.; Pashchenko, V.; Pashchenko, A.; Shemjakov, A.; Varyukhin, V.; Prilipko, S.; Mikhaylov, V.; Kravchenko, Z.; Szytua, A.; Bazela, W. Nanoparticle Size Effect on the Magnetic and Transport Properties of (La0.7 Sr0.3)0.9 Mn1.1 O3 Manganites. *Low Temp. Phys.* **2009**, *35* (7), 568–576. https://doi.org/10.1063/1.3170933.

(104) Aurélio, D.; Mikšátko, J.; Veverka, M.; Michlová, M.; Kalbáč, M.; Vejpravová, J. Thermal Traits of MNPs under High-Frequency Magnetic Fields: Disentangling the Effect of Size and Coating. *Nanomaterials* **2021**, *11* (3), 1–11. https://doi.org/10.3390/nano11030797.

(105) Chinnasamy, C. N.; Yang, A.; Yoon, S. D.; Hsu, K.; Shultz, M. D.; Carpenter, E. E.; Mukerjee, S.; Vittoria, C.; Harris, V. G. Size Dependent Magnetic Properties and Cation Inversion in Chemically Synthesized Mn Fe2 O4 Nanoparticles. *J. Appl. Phys.* **2007**, *101* (9), 1–4. https://doi.org/10.1063/1.2710218.

(106) Spinu, L.; Srikanth, H.; Carpenter, E. E.; O'Connor, C. J. Dynamic Radio-Frequency Transverse Susceptibility in Magnetic Nanoparticle Systems. *J. Appl. Phys.* **2000**, *87* (9), 5490–5492. https://doi.org/10.1063/1.373381.

Vitae

Meg Thornton was born in Richmond, Virginia in 1996. She received her B.S. in Chemistry with a Professional Chemist concentration and Mathematics minor from Virginia Commonwealth University in 2018. During her undergraduate studies, she competed on the Equestrian Team of VCU, was an active member of Phi Mu Fraternity, and conducted an independent study with Dr. Alenka Luzar and Dr. Dusan Bratko conducting molecular simulations on pentagraphene. In 2018, she entered graduate school at Virginia Commonwealth University to pursue a Ph.D. in inorganic chemistry. During her studies, she completed an internship at NASA Langley Research Center in molecular modeling and another with the VCU Innovation Gateway as a Licensing Liaison, and served as a member of the Student Government Association Independent Financial Board.